

1 **High mid-Holocene accumulation rates over West Antarctica inferred from
2 a pervasive ice-penetrating radar reflector**

3
4 Julien A. Bodart¹, Robert G. Bingham¹, Duncan A. Young², Joseph A. MacGregor³, David
5 W. Ashmore^{4,5}, Enrica Quartini^{2,6}, Andrew S. Hein¹, David G. Vaughan^{6,7,†}, and Donald D.
6 Blankenship²

7
8 ¹School of GeoSciences, University of Edinburgh, Edinburgh, UK

9 ²Institute for Geophysics, University of Texas at Austin, Austin, Texas, USA

10 ³Cryospheric Sciences Laboratory, NASA Goddard Space Flight Center, Greenbelt, Maryland, USA

11 ⁴School of Environmental Sciences, University of Liverpool, Liverpool, UK

12 ⁵MET Office, Exeter, UK

13 ⁶Department of Astronomy, Cornell University, Ithaca, New York, USA

14 ⁷British Antarctic Survey, Cambridge, UK

15 [†]Deceased

16
17
18 Correspondence to: Julien A. Bodart (julien.bodart@ed.ac.uk)

19
20 **Key points**

21
22
23 • We estimate mean accumulation rates for the past ~5000-4700 years across the Pine Island,
24 Thwaites, and Institute and Möller ice-stream catchments in West Antarctica using a
25 ubiquitous, ice-core dated internal radar-sounded and ice core-dated Internal Reflecting
26 Horizon reflection

27 • Accumulation rates were 18% higher during the mid-Holocene compared to modern rates
28 over the Amundsen-Weddell-Ross Sea divide

29 • Spin-up of regional and continental ice-sheet models Spin-up of ice sheet models must should
30 account include for time-varying changes in Holocene accumulation rates from the WAIS
31 Divide Ice Core between the Last Glacial Maximum and the present to generate more realistic
32 grounding-line evolution and past sea level rise contribution across this region

34 **Abstract**

35
36 Modelling Understanding the past and future evolution of the Antarctic Ice Sheet the West Antarctic
37 Ice Sheet (WAIS) to atmospheric and ocean forcing is challenged by the availability and quality of
38 observed palaeo-boundary conditions. Numerical ice-sheet models often rely on these palaeo-boundary
39 conditions to guide and evaluate their models' predictions of sea-level rise, with varying levels of
40 confidence due to the sparsity of existing data across the ice sheet. A key potential data source for
41 large-scale reconstructing reconstruction of past ice-sheet processes on large spatial scales are Internal
42 Reflecting Horizons (IRHs) detected by Radio-Echo Sounding (RES) techniques. When isochronal and
43 dated at ice cores, IRHs can be used to determine palaeo-accumulation rates and patterns therein. Using
44 a spatially extensive IRH over Pine Island Glacier, Thwaites Glacier, and Institute and Möller Ice
45 Streams (covering a total of 610 000 km² or 30% of the WAIS), and a local layer approximation model,
46 we infer mid-Holocene accumulation rates over the slow-flowing parts of these catchments for the past
47 ~475000 years. By comparing our results with modern climate reanalysis models (1979–2019) and
48 observational syntheses (1651–2010), we estimate that accumulation rates over the Amundsen-
49 Weddell-Ross divide were on average 18% higher during the mid-Holocene than modern rates during
50 the mid-Holocene. However, no significant spatial changes in the accumulation pattern were observed.
51 These higher mid-Holocene accumulation-rate estimates match previous palaeo-accumulation
52 estimates from ice-core records and targeted RES surveys over the ice divide, and they also coincide
53 with periods of grounding-line re-advance during the Holocene over the Weddell and Ross Sea sectors.
54 We find that our spatially-extensive, mid-Holocene-to-present accumulation estimates are consistent
55 with a sustained late-Holocene period of higher accumulation rates occurring over millennia at the
56 WAIS Divide Ice Core, thus highlighting the spatial representativeness of this ice core to the wider
57 West Antarctic region. Our results highlight the need for ice sheet models to account for time-varying
58 accumulation rates across the WAIS during the Holocene to provide better estimates of its contribution
59 to past sea level rise. We conclude that future regional and continental ice-sheet modelling studies
60 should base their climatic forcings on time-varying accumulation rates from the WAIS Divide Ice Core
61 through the Holocene to generate more realistic predictions of the West Antarctic Ice Sheet's past
62 contribution to sea-level rise.

63
64
65 **Key words:** West Antarctica, Internal Reflecting Horizons, Accumulation, Holocene, Ice-Penetrating
66 Radars, Ice-Core, Pine Island Glacier, Thwaites Glacier.

68 **1. Introduction**

69 Improving our knowledge of past climatic changes over the West Antarctic Ice SheetAntarctic Ice
70 Sheet(WAIS) is required if we are to understand its present evolution and model its future under
71 increasingly rapid climatic changes (IPCC, 2021). Most studies of past ice-sheet behaviour over
72 Antarcticathe WAIS have focused on modelling changes in ice volume and grounding-line (GL)
73 retreat following the Last Glacial Maximum (LGM, ~20 ka Before Present, BP) (Denton and Hughes,
74 2002; Golledge et al., 2012; 2013; Hillenbrand et al., 2013; 2014; Le Brocq et al., 2011; Kingslake et
75 al., 2018); however, less attention has been paid to ice-sheet evolution during the Holocene (~11.7 ka
76 BP to present). Recent evidence suggests that the parts of the grounding line of West Antarctica GL
77 may have retreated several hundred kilometres inland from its current position at ~10 ka and
78 subsequently re-advanced to reach its modern position sometime during the Holocene, due to isostatic
79 rebound and climate-induced changes, particularly over the Weddell Sea and western Ross Sea
80 sectors (Siegent et al., 2013; Bradley et al., 2015; Kingslake et al., 2018; Wearing and Kingslake,
81 2019; Venturelli et al., 2020; Neuhaus et al., 2021; Johnson et al., 2022). However,

82 ~~the inland~~ atmospheric and ice-dynamical conditions further inland, which may could also have
83 induced have partly caused this Holocene grounding-line GL migration, remain relatively under-
84 studied poorly constrained. An early investigation by Whillans (1976) using radar data near Byrd Ice
85 Core indicated stability during the Late Pleistocene and Holocene epochs and late Pleistocene.
86 Records of temperature and precipitation from the WAIS Divide Ice Core (hereafter abbreviated as
87 WD14; Fig. 1) in the central WAIS-West Antarctic Ice Sheet (WAIS) suggest higher accumulation
88 rates during the Holocene than the at present (Fudge et al., 2016), a trend that is also observed across
89 small parts of the Western divideAmundsen-Weddell-Ross divide (hereafter referred to as WD; Fig.
90 1) near the WAIS Divide Ice Core (hereafter referred to as WD14; Fig. 1WD14)-where isolated
91 Radio-Echo Sounding (RES) surveys have shown 15-30% higher accumulation rates during the mid-
92 Holocene compared to modern values (Siegent and Payne, 2004; Neumann et al., 2008; Koutnik et al.,
93 2016).

94 At present modellingMany numerical ice-sheet modelsstudies that aim to predict Antarctica's
95 future long-term (past and future) changescontribution to sea-level riseover the WAIS use past ice-
96 sheet reconstructions from after the LGM to guide and evaluate their models (Chavaillaz et al., 2013;
97 DeConto and Pollard, 2016; Bracegirdle et al., 2019). However, even well-used ice-sheet
98 reconstructions assume that the ice sheet retreated continuously throughout the Holocene (e.g.
99 RAISED Consortium, 2014), a finding that has been challenged recently for the WAIS (e.g.
100 Kingslake et al., 2018). HoweverFurther, significant discrepancies between model simulations and the
101 palaeo-proxy record currently impede our ability to predict confidently how the ice sheet will respond
102 to future changes in the climate (e.g. Johnson et al., 2021). While improvements in model physics
103 parameterisations and parameterisations are needed to close this gap (Bracegirdle et al., 2019; Sutter
104 et al., 2021), a considerable improvement in the availability and quality of palaeo-proxy records,
105 particularly during the Holocene, is also needed to provide better constraints for ice-sheet models and
106 ultimately gain better resolve a more accurate picture of the past ice-sheet changes (Kingslake et al.,
107 2018; Jones et al., 2022). Palaeo-proxy data over the WAIS have traditionally come from point-based
108 measurements, such as ice cores (e.g. Petit et al., 1999; Parrenin et al., 2007; WAIS Divide Project
109 Members, 2013; ~~;~~ Cuffey et al., 2016; McConnell et al., 2017; Buizert et al., 2021), sediment cores
110 (e.g. Hillenbrand et al., 2013; Arndt et al., 2017; Hillenbrand et al., 2017; Kingslake et al., 2018;
111 Venturelli et al., 2020; Neuhaus et al., 2021; Sproson et al., 2022), or fromsurface-exposure dating
112 (e.g. Stone et al., 2003; Suganuma et al., 2014; Johnson et al., 2014; Hein et al., 2016; Nichols et al.,
113 2019; Johnson et al., 2020; Braddock et al., 2022).

114 A complimentary and spatially extensive alternative data source for inferring past climate
115 across an ice sheet is provided by Internal Reflecting Horizons (IRHs) detected by RES. They

116 primarily result from englacial acidity contrasts sounded by RES and are often detected horizontally,
117 for hundreds of kilometres on RES data can be traced horizontally across large parts of the ice sheet
118 on RES profiles (Harrison, 1973; Bingham and Siegert, 2007), thus making them a useful resource to
119 infer past climates on regional to continental scales (Bingham and Siegert, 2007; Harrison, 1973).

120 When employed in combination with ice-core stratigraphy, IRHs can be used to extrapolate age-depth
121 relationships across large spatial scales away from an ice core by following peaks in
122 electromagnetic power in the radar data (e.g. Beem et al., 2021; Bodart et al., 2021a; Cavitte et al.,
123 2016; Jacobel and Welch, 2005; MacGregor et al., 2015; Whillans, 1976; Winter et al., 2019).

124 In comparison contrast to East Antarctica and Greenland, extrapolating IRH extension of past
125 ice sheet records from WAIS ice cores to entire glacier catchments has so far been challenging due to
126 the limited availability of fewer deep ice cores there and, until recently, the lack of suitable well-dated
127 IRH datasets. However, efforts have intensified in recent years to improve our understanding of the
128 ice stratigraphy over this sector. In particular, four recent studies using airborne RES data over the
129 WAIS (Karlsson et al., 2014; Muldoon et al., 2018; Ashmore et al., 2020a; Bodart et al., 2021a) all
130 identified a particularly distinct and bright IRH precisely dated using the Byrd and WD14 ice-core
131 chronologies at 4.72 ± 0.28 ka BP (Muldoon et al., 2018; Bodart et al., 2021a). A comparison
132 with volcanic sulphate deposition within the WD14 and Siple Dome ice cores revealed a large peak
133 in sulphate concentration matching the age and depth of this ubiquitous layer IRH (Kurbatov et al.,
134 2006; Bodart et al., 2021a; Cole-Dai et al., 2021; Sigl et al., 2022), which is hereafter termed the
135 "4.72 ka IRH". This IRH has now been observed by multiple RES systems from different surveys and
136 data providers. It and extends throughout much of the slower-flowing ice of the Amundsen and
137 Weddell Sea embayments ($< 400 \text{ m a}^{-1}$), including across the divides demarcating regions draining
138 into the Amundsen, Weddell and Ross Seas.

139 Despite their potential wide-ranging applications, the incorporation of IRHs into ice-sheet
140 models has so far been limited compared to other types of palaeo-proxy data, primarily because the
141 inference of accumulation-rate or ice-flow history from IRHs is an ill-posed inverse problem
142 (Waddington et al., 2007). Previous applications using IRHs to inform regional and continental
143 models include: (a) constraining decadal-scale Surface Mass Balance (SMB) estimates from
144 atmospheric models using annually-resolved IRHs found in the shallow firm (Medley et al., 2013;
145 2014; Van Wessem et al., 2018; Dattler et al., 2019; Kaush et al., 2020; Cavitte et al., 2022); (b)
146 inferring past accumulation rates going back further in time (i.e. 100s to 1000s years) with the aim of
147 comparing past accumulation estimates with modern times (e.g. Leysinger Vieli et al., 2004; Siegert
148 and Payne, 2004; Neumann et al., 2008; MacGregor et al., 2009, 2016; Leysinger Vieli et al., 2011;
149 Cavitte et al., 2018); or (c) integrating both their characteristics (e.g. elevation in the ice) and the
150 information inferred from them (e.g. accumulation or basal-melt rates) to evaluate the output from
151 regional and continental ice-sheet models (Leysinger Vieli et al., 2011; 2018; Holschuh et al., 2017;
152 Sutter et al., 2021). Promisingly, Sutter et al. (2021) recently showed that spatially extensive Antarctic
153 IRHs can provide unique benchmarks for constraining ice-sheet model parameterisations (i.e. climate
154 forcing and simulated ice flow), which are then used to simulate palaeo ice-sheet evolution. Together,
155 these studies indicate multiple avenues for ice-sheet models to assimilate IRHs further improve
156 estimates of past, current and future ice-sheet changes.

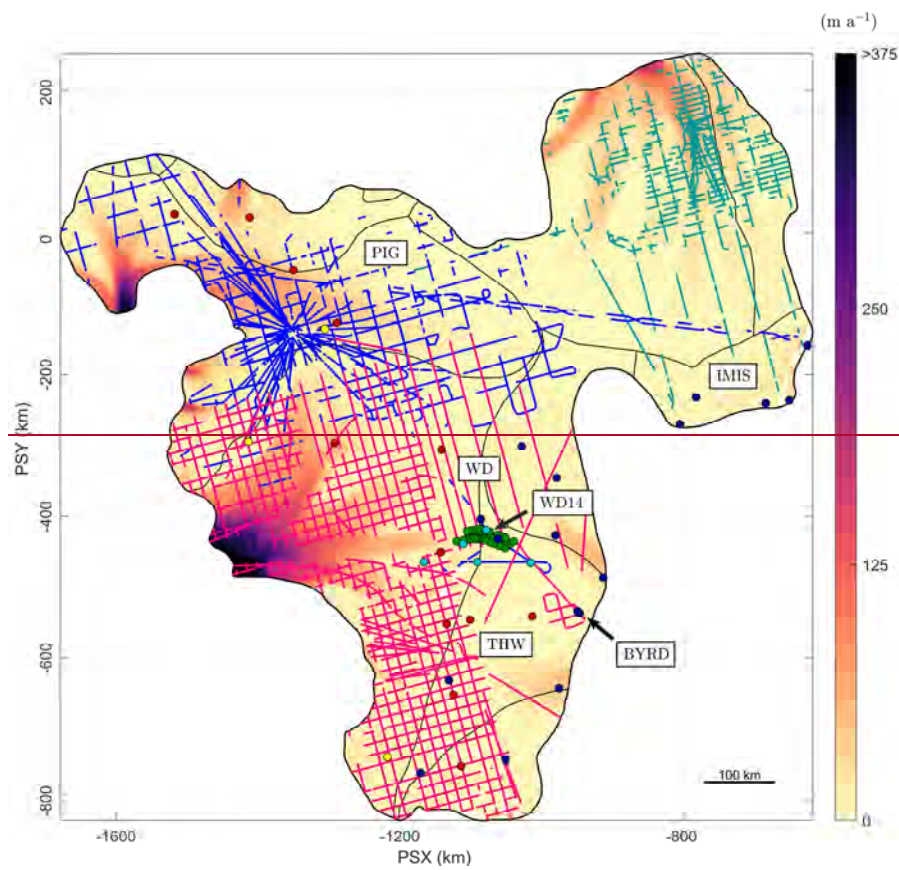
157 Here, our aim is to estimate mid-Holocene accumulation rates across the WAIS from first-
158 order calculations using a one-dimensional (1-D) model, local-layer approximation (LLA) model
159 (Waddington et al., 2007), informed constrained by the spatially extensive 4.72 ka IRH. We first
160 describe the data, the model used and their limitations and uncertainties. We first describe the data and
161 the 1-D model, and discuss the methods used to assess the feasibility of the LLA from gradients in
162 horizontal ice flow, ice thickness and accumulation rate and how these translate into accumulation
163 rate uncertainties (Sect. 2). We then present our accumulation-rate estimates and discuss the
164 effects of spatial and topographic controls on our results in relation to observed and modelled modern
165 accumulation rates using both modelled gridded data from the Regional Atmospheric Climate Model

167 2 (hereafter RACMO2; Van Wessem et al., 2018) and observational point-based data from snow, firm
168 and ice cores (Neumann et al., 2008; Burgener et al., 2013; Favier et al., 2013; Mayewski and Dixon,
169 2013; Medley et al., 2014), to generate reveal a longer-term perspective on changes between the mid-
170 Holocene and the present (Sect. 3). Finally, we place our results in the context of previous studies that
171 consider WAIS the evolution of the WAIS during the Holocene (Sect. 4).

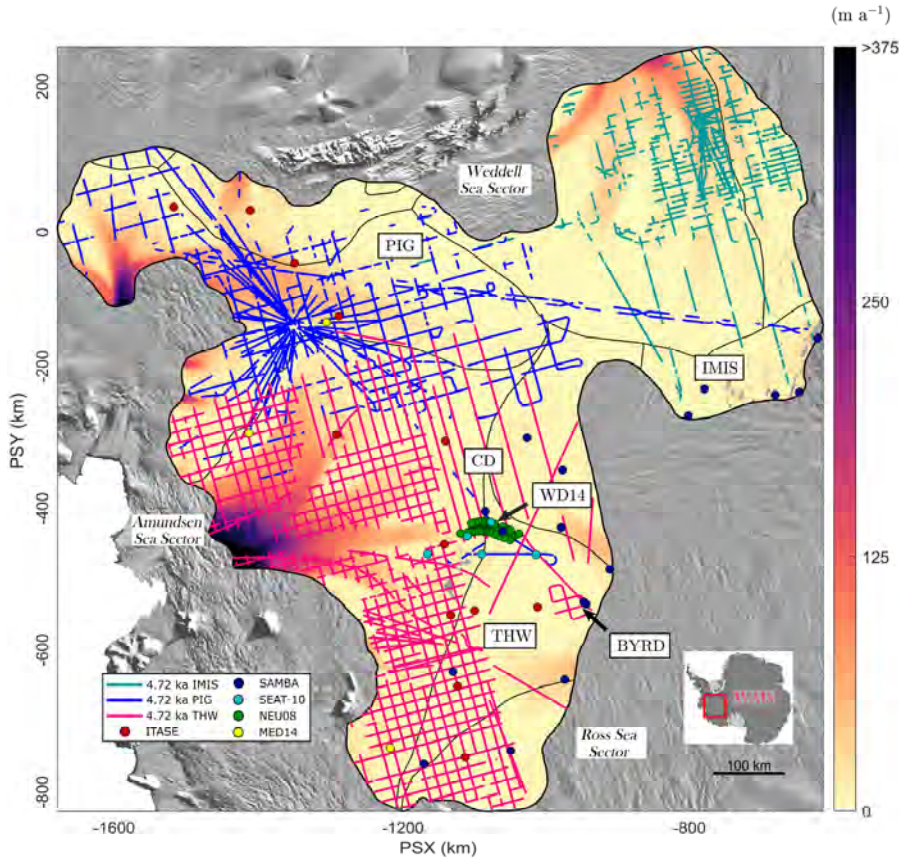
172 **2. Datasets and methods**

173 **2.1 Along-track IRH data**

175 We used data from extensive (~91 000 flight-track km) RES surveys acquired across West
176 Antarctica between 2004 and 2018. The main contributing surveys are the University of Texas
177 Institute for Geophysics (UTIG) 2004-2005 AGASEA survey flown over Thwaites Glacier (THW)
178 and Marie Byrd Land which deployed the 60-MHz High Capability Airborne Radar Sounder
179 (HiCARS) radar system (Holt et al., 2006; Peters et al., 2007), and the British Antarctic Survey (BAS)
180 2004-05 BBAS survey over Pine Island Glacier (PIG) and 2010-2011 IMAFI survey over Institute
181 and Möller Ice Streams (IMIS) which deployed the 150-MHz Polarimetric Airborne Survey
182 INstrument (PASIN) radar system (Vaughan et al., 2006; Corr et al., 2007; Ross et al., 2012;
183 Fréemand, Bodart et al., 2022) (Fig. 1; Table 1). Additional profiles from NASA's Operation Ice
184 Bridge (OIB; MacGregor et al., 2021) 2016 and 2018 surveys, flown with the 190-MHz Multichannel
185 Coherent Radar Depth Sounder 2 (MCoRDS-2) radar system (CReSIS, 2018), were also used to
186 extract IRH information near the WD14 Ice Core and upper IMIS catchments (Bodart et al., 2021a;
187 Figure 1 and Table 1). We refer the reader to the above references for comprehensive details on each
188 system's capabilities.



189



190
191 Figure 1. Map of the datasets and key locations in this study. The three datasets that contain the 4.72 ka
192 IRH are colour-coded as IMIS (green), PIG (blue), and THW (pink). IRH ~~data falling outside where $D \gg 1$~~
193 ~~are excluded~~ (see Section 2.2.1; Figure S1) ~~are excluded~~. Points ~~on the map~~ represent the snow, firn and ice
194 cores used in this study to compare modern ~~accumulation~~ rates of accumulation with ~~our~~ ~~those inferred from the~~
195 ~~4.72 ka IRH-to-present estimates~~ (see Section 2.4 for source references). The background colour map shows
196 modern surface speeds from Rignot et al. (2017). Locations mentioned in this paper are abbreviated on the map,
197 as follows: BYRD (Byrd Ice Core), IMIS (Institute and Möller Ice Streams), PIG (Pine Island Glacier), THW
198 (Thwaites Glacier), WAIS (West Antarctic Ice Sheet), WD-CD (Central Amundsen-Weddell-Ross
199 DivideWestern Divide), WD14 (WAIS Divide Ice Core). Major ice divides are from Mouginot et al. (2017).
200 The background image is the 2014 MODIS mosaic of Antarctica (Haran et al., 2018). For all analysis and
201 figures in this study, the projection for all figures in this paper is WGS84/SCAR Antarctic Polar Stereographic
202 projection is used (PSX/PSY; EPSG: 3031).

203 These RES surveys were used to track and date six IRHs spanning ~~much of the Late~~
204 ~~Pleistocene and Holocene and Late Pleistocene (25.7 – 2.3 ka BP) that collectively covering much of~~
205 ~~the WAIS across including~~ IMIS (Ashmore et al., 2020a), PIG (Karlsson et al., 2014; Bodart et al.,
206 2021a) and THW (Muldoon et al., 2018), ~~collectively spanning much of the WAIS~~. Here we only
207 consider the 4.72 ka IRH mapped in all ~~three four~~ studies and shown in Figure 1, as it is by far both
208 the most spatially extensive and the only commonly traced IRH across all studies. We first merged all
209 data points from the 4.72 ka IRH across the three catchments, resulting in a cumulative distance of

210 ~40 000 line-km of IRH profiles (44% of the RES surveys' total coverage; Table 1). Although the
 211 along-track RES data were acquired with a trace spacing of between 10 and 35 m, depending on the
 212 dataset used, we re-sampled these points to 500 m in the along-track direction. We then added a
 213 spatially invariant firm correction of 10 m onto the Muldoon et al. (2018) dataset to match the same
 214 firm correction applied by the other studies to correct the IRH depth.
 215 Finally, we calculated the median value of all ice thicknesses and IRH depths falling within ~~the nearest~~ 500 m interval.

216 Table 1. Characteristics of each IRH dataset used in this study that contain the 4.72 ka IRH. 'Reflector
 217 1' in Muldoon et al. (2018) is abbreviated here as 'R1'.

Survey name	Survey provider	RES system	Dataset reference	Cumulative IRH distance (10^3 km)
IMAFI	BAS	PASIN 150-MHz	H2 in Ashmore et al. (2020a)	1.5×10^4
BBAS / OIB	BAS / NASA	PASIN 150-MHz / MCoRDS-2 190 -MHz	R2 in Bodart et al. (2021a)	0.6×10^4
AGASEA	UTIG	HiCARS 60-MHz	R1 in Muldoon et al. (2018)	1.9×10^4

218 2.2 Inferring accumulation rates

219 To infer accumulation rates from the 4.72 ka IRH, we used the Nye model, a 1-D ice-flow
 220 model widely used for estimating accumulation rates and age-depth relationships over relatively slow-
 221 flowing parts of an ice sheet (Nye, 1957; Fahnestock et al., 2001a). This model invokes the local-layer
 222 approximation (LLA), i.e. it assumes that the time-averaged accumulation rate that the IRH has
 223 experienced since its upstream inception at the surface can be adequately represented by its depth
 224 where it is observed presently. Other 1-D models exist, including the Dansgaard-Johnsen (Dansgaard
 225 and Johnsen, 1969) and the shallow-strain rate model (MacGregor et al., 2016), but ~~neither~~ were less
 226 suitable for estimating accumulation rates here this study due to uncertainty~~ies~~ in the basal shear layer
 227 thickness across our survey area and because we are limited to only one IRH to constrain the ice-flow
 228 model respectively. The Nye model assumes that ice thickness is constant and therefore that the ice
 229 sheet has been in a steady state since the deposition of the IRH, an realistic acceptable assumption for
 230 the period under investigation here. The Nye model states:
 231

$$232 \dot{b}_a = \ln \left(\frac{z_a}{H} \frac{H}{a} \right), \quad (1)$$

233 where \dot{b}_a is the mean ~~surface~~-accumulation rate during the Holocene epoch between an IRH of age a
 234 and the present, z_a represents the depth of the IRH dated at the ice core, and H is the ice thickness.
 235 The model assumes that the vertical strain rate, $\dot{\varepsilon}_{zz}$, is also constant and vertically uniform, so that it
 236 exactly balances the overburden of local ice accumulation:
 237

$$238 \dot{\varepsilon}_{zz} = \frac{\dot{b}_a}{H}. \quad (2)$$

239 We iterated Eq. (1) over the re-sampled 500-m spaced dataset using the depth of the 4.72 ka
 240 IRH for z_a and used the median radar-derived ice-thickness measurement re-sampled over the 500-m
 241 grid to obtain H , when this information was available. In areas where the radar did not sound the bed,
 242 we used the BedMachine Antarctic v2 gridded product to obtain a value for H (Morlighem, 2020).
 243 Note that ~~the~~-accumulation rate values presented in this study are all reported in m a^{-1} of ice
equivalent.

244 Uncertainties in accumulation rates are calculated by iterating Eq. (1) using the lowest and
245 highest possible age of the 4.72 IRH based on the maximum and minimum age uncertainty (± 0.28 ka)
246 calculated from RES and ice-core depth uncertainties (see details in Muldoon et al. (2018) and Bodart
247 et al. (2021a)). This results in lower and upper bounds in accumulation rates over our model domain
248 (Fig. S2a b), which are then combined to provide a relative uncertainty in accumulation rates for the
249 4.72 ka IRH (Fig. S2c). The maximum relative uncertainty in accumulation rates for the 4.72 ka IRH
250 is 3.3%, with a median value of $<0.5\%$ across our grid. Note that these values do not include
251 uncertainties due to the model approximation itself. As discussed in the next two sections, we believe
252 model uncertainties to be small for the domain considered.

253 2.2.1 Assessing the suitability of the 1-D model

254 To quantify the suitability of the LLA ~~onto from which the our accumulation rates 1-D model~~
255 is are based, we calculated the effects of horizontal gradients in modern ice thickness and
256 accumulation rates along particle paths in their ability to affect IRH depths ~~across our grid~~, as per
257 Waddington et al. (2007). ~~In places wW~~here these gradients are ~~too~~ large, estimates of accumulation
258 rates from IRHs likely require a more complete treatment of ice flow ~~and strain rates and its effect~~
259 upon to account for disturbances in IRH depths, which ~~only~~ multi-dimensional models and more
260 physically complete models can better are able to resolve (e.g. Waddington et al., 2007; Leysinger
261 Vieli et al., 2011; Karlsson et al., 2014; Nielsen et al., 2015; Koutnik et al., 2016; MacGregor et al.,
262 2016). However, such models are significantly more computationally expensive over such a larger
263 area and depend on well-constrained boundary conditions from along-flow radar profiles which are
264 not often available at an ice-sheet level (MacGregor et al., 2009).

265 We quantified ~~stimat~~ To quantify the effect of horizontal gradients on an IRH of age a ~~by first~~
266 ~~estimating, we computed~~ the total horizontal particle path length L_{path} ~~each “particle” of the 4.72 ka~~
267 ~~IRH has travelled since a , and then the~~ characteristic lengths of variability in ice thickness (L_H) and
268 apparent accumulation rate (L_b) ~~representing the gradients in ice thickness and accumulation rates~~
269 ~~respectively for age a~~ (Supplementary Information). These three components were then combined to
270 generate a non-dimensional parameter D (Fig. S1d), which we used as a confidence metric for our
271 inferred accumulation rates. Both Waddington et al. (2007) and MacGregor et al. (2009) suggested a
272 value of $D \ll 1$ over Antarctica, whereas MacGregor et al. (2016) used a maximum value of $D = 1$
273 value of unity to estimate where the LLA is acceptable over Greenland, but because the value of D
274 ~~cannot yet be translated~~ simply quantitatively into an uncertainty value for in an LLA-inferred
275 accumulation rate, it is not yet clear what exact value is appropriate. Smaller values of D indicate that
276 local horizontal gradients in ice thickness and accumulation rates have a smaller effect on IRH depth
277 of age a , and thus ~~we can assume that that~~ the LLA ~~is may be~~ valid (Waddington et al., 2007;
278 MacGregor et al., 2009; 2016). However ~~Where, if~~ $D \gg 1$, the depth of the an IRH is less likely to be
279 unlikely not necessarily the result of to be the sole result of accumulation rates at the surface or
280 vertical strain rates further down, and thus that a more sophisticated model is thus likely required
281 (Sect. 2.2.2) (Waddington et al., 2007). However, MacGregor et al. (2009) found that even along a
282 flowband across Lake Vostok where the mean value of D is 0.50 for a 41-ka IRH, the difference in
283 accumulation rate inferred from the LLA and from a more sophisticated flowband model could be
284 relatively small (4-16%). This similarly suggests that accumulation rate can be inferred acceptably
285 using the LLA where D is higher.

286 In our case ~~For our study area, most of the survey areas has~~ D values ~~are mostly that are~~ well
287 below ~~the~~ unity (median: 0.19; 25th quartile: 0.09; 75th quartile: 0.34), which suggests relatively little
288 effect from ice-dynamical processes upon IRH depths across most of our grid. We used the upper
289 quartile of the D distribution across our model domain (i.e. $D \leq 0.34$) to show areas where we can
290 have confidence that accumulation rate remains the dominant factor influencing the vertical position
291 of our IRHs in the ice column (i.e. where the $D \ll 1$ criterion is likely met; see Fig. Fig. 4, S1d). While

292 accumulation rates inferred from IRHs situated in the upper quartile (see Fig. S1d) may still be valid,
293 we suggest additional caution in interpreting our results there due to the potential impact of larger
294 flow gradients on IRH depths, a limited number of IRH profiles near the onset of PIG's tributaries and
295 over THW's central trunk, which we excluded from our analysis.

296 **2.2.2 Model limitations and uncertainty**

297 One of the main limitations of the Nye model is that it assumes that gradients in sliding
298 velocity are mostly concentrated in a thin layer at the ice-bed interface and that the ice column
299 deforms by pure shear only (Nye, 1957; Fahnestock et al., 2001a). For this reason, the Nye model is
300 generally only appropriate for IRHs found in the upper part of the ice column, as is the case here.
301 Additionally, the use of the model is restricted to areas where ice flow is relatively slow and
302 horizontal strain rates are also relatively low.

303 Here we focus on a shallower IRH situated in the upper part of the ice column (median: 40%;
304 25th quartile: 30%; 75th quartile: 50%; Fig. 2b-c), for which we can reasonably assume that the ice
305 sheet has remained close to steady state and where IRHs are likely shallow enough not to have
306 experienced appreciable flow disturbances that would affect the Nye model assumptions.
307 Additionally, due to the inherent nature of tracking IRHs through RES data, our coverage is limited to
308 areas where ice-flow speeds are relatively low and IRHs are undisturbed.

309 Whilst this is the case for most of our IRH coverage, in some portions of our study area, we
310 note that some of the IRH is found deeper in the ice column and/or in faster-flowing areas as sections of the
311 ice sheet (e.g. in the downstream sectors of our grid, Fig. 1-2b-c); areas where the assumptions that
312 the 1-D model is based on may be challenged.

313 Multi-dimensional models would likely improve the accumulation estimates for IRHs found
314 in the lower half of the ice column or in more disrupted or faster flowing areas (e.g. Waddington et
315 al., 2007; Neumann et al., 2008; MacGregor et al., 2009; Leysinger Vieli et al., 2011; Karlsson et al.,
316 2014; Nielsen et al., 2015; Koutnik et al., 2016; Sutter et al., 2021); however, they are much more
317 computationally expensive and depend on well constrained boundary conditions from along-flow
318 radar profiles which are not often available over such large regions (MacGregor et al., 2009).

319 However, here, we focus on a shallower IRH situated within the upper 40% part of the ice column
320 (median: 40%; 25th quartile: 30%; 75th quartile: 50%; Fig. 2b-c), where we can be reasonably
321 confident that the ice sheet has remained close to steady state and where IRHs are likely shallow
322 enough not to have sustained appreciable disturbances that would affect the Nye model assumptions
323 (Sect. 2.2.3).

324 Additionally, due to the inherent nature of tracking IRHs through RES data, our coverage is
325 limited to areas where ice-flow speeds are relatively low and IRHs can be considered are relatively
326 undisturbed. An assessment of strain rates over our model domain suggests limited disturbance over
327 the WD and most of our grid, apart from near the onset of faster flow at the boundaries of our grid
328 with the trunks of PIG and THW where higher strain rates are observed (Fig. S23). This pattern,
329 combined with the assessment of the suitability of the LLA (Sect. 2.2.1) and exclusion of IRHs
330 outside of the $D > 1$ boundary, supports our application of a 1-D modelling approach here.

331 Estimating uncertainty in accumulation rates from the Nye model is non-trivial. Previous
332 studies have used the misfit between the accumulation rate calculated using multiple proximal IRHs
333 in the ice column (e.g. Fahnestock et al., 2001a; 2001b; Leysinger Vieli et al., 2004; MacGregor et al.,
334 2016). Unfortunately, this method is not suitable here due to the dearth of spatially extensive IRHs
335 younger than 4.72 ka over our model domain.

336 Instead, uncertainty in the Nye-inferred accumulation rates were calculated using: (a) the
337 lowest and highest possible accumulation rates from Eq. (1) using the age uncertainty (± 0.28 ka) of
338 the 4.72 ka IRH and (b) the lowest and highest possible accumulation rates inferred from an additional
339 1-D model (Eq. S5) which accounts for the effect of strain rates on accumulation rates (i.e. the
340 shallow-strain rate model from MacGregor et al. (2016); Supplementary Information; Fig. S2-4).

341 This calculation provides lower and upper bounds for the IRH-inferred accumulation rates
342 (Fig. S4a-b), which were then averaged to generate a relative uncertainty (Fig. S4c). From this
343 assessment, we estimate a median relative uncertainty in the Nye-inferred accumulation rates for the
344 4.72 ka IRH of 14% across our grid. This uncertainty is higher in the downstream edges of our grids,
345 particularly over the PIG, THW and IMIS catchments, and generally low over the Amundsen-
346 Weddell-Ross divide (Fig. S4), reflecting the effect of spatially variable strain rates on the inferred
347 accumulation rates. When combined with the assessment of the suitability of the LLA and exclusion
348 of IRHs where the $D > 1$ (Sect. 2.2.1-2.2.2), we conclude that it supports our application of a 1-D
349 modelling approach here.

350 2.3 Gridding and filtering

351 Once IRH depths and accumulation rates for the 4.72 ka IRH were obtained at regular 500-m
352 points along RES flight paths, we filtered the results using a moving-average Gaussian filter of length
353 30 samples (equivalent to ~ 15 km) to reduce along-track noise in the IRH depth, and then gridded the
354 filtered result using a Delaunay-triangulation-based natural neighbour interpolation method onto a 1-
355 km polar stereographic grid. We further smoothed the gridded data using an 18-km square cell mean
356 filter to limit the localised interpolation artefacts arising from the interpolation, which can be
357 problematic in areas with poor data survey coverage. Figure S54 shows the maximum distance
358 away from the nearest 500-m along-track point used to produce Figures 2-3, and thus where errors in
359 the interpolated grids are expected to be larger. The median value of this maximum distance is 5 km
360 and its maximum value is 75 km, which is comparable to previous studies that infer Surface Mass
361 Balance (SMB)-SMB from IRHs in the shallow firm (e.g. Medley et al., 2014). We evaluated other
362 possible interpolation methods (e.g., kriging and using different semi-variogram models), but they
363 resulted in similar or poorer quality, and were thus discounted.

364 2.4 Comparison with modern observations

365 To compare our inferred accumulation estimates for the past 4.72 ka with modern values
366 times, (defined here as 1651-2019), we derived information on modern accumulation rates from two
367 sources, one modelled (gridded) and one from a series of observational (point-based) datasets.

368 We used modelled gridded accumulation rates from the Regional Atmospheric Climate Model
369 2.3p2 (hereafter RACMO2) RACMO 2.3p2-1979-2019 Surface Mass Balance (SMB) product forced
370 at its margin with the ERA-Interim product (native resolution: 27 km) as an estimate for modern
371 accumulation rates (Van Wessem et al., 2018). Although SMB is not technically equivalent to the
372 accumulation rate, runoff and sublimation are negligible in our survey area (Medley et al., 2013) so
373 we consider assume SMB is equal to accumulation rate in this region. We converted modelled values
374 from $\text{kg m}^{-2} \text{a}^{-1}$ to m a^{-1} of ice equivalent using an ice density value of 917 kg m^{-3} , calculated the 40-
375 year mean, and then bi-linearly interpolated the gridded RACMO2 product to the same 1-km grid
376 resolution as our 4.72 ka-to-present accumulation grid (Sect. 2.3) to ensure consistency when
377 comparing both datasets.

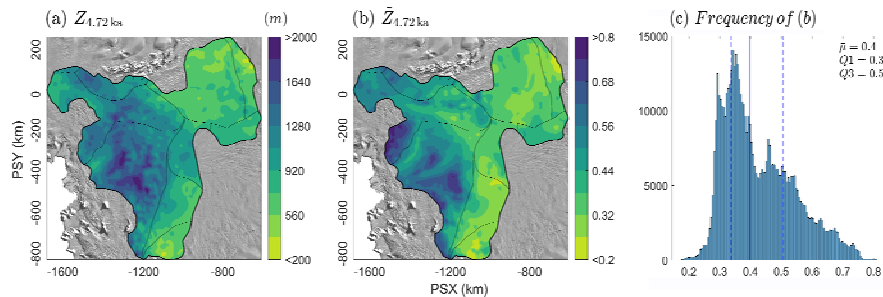
378 Observational point-based measurements were obtained from a series of snow, firn and ice
379 cores from the ITASE (Mayewski and Dixon, 2013), MED14 (Medley et al., 2014), SAMBA (Favier
380 et al., 2013), and SEAT-10 (Burgener et al., 2013) datasets, as well as from a network of centennial-
381 averaged modern accumulation rates derived from shallow IRHs traced on ground-based RES data
382 over the central divide WD and dated using a shallow ITASE Ice Core (Neumann et al., 2008) (Fig.

383 1). This [results resulted](#) in 79 point-based accumulation measurements [from cores](#) covering the period
 384 1651-2010 CE (Common Era) and spread across our model domain (see Figure 1). Further detail on
 385 these datasets can be found in the above references.

386 To compare the Holocene gridded product with the point-based measurements, we first
 387 calculated the average value of the accumulation rate at the point measurement for the entire period.
 388 We converted [these](#) values to ice-equivalent accumulation rates [\(as above\)](#) and [then](#) extracted [the](#)
 389 two paired values, i.e., the value for the point-measurement for modern accumulation rates and the
 390 value for the nearest grid cell in the gridded 4.72 ka-to-present accumulation estimates to this
 391 measurement.

392 3. Results

393 The final grids for depth and accumulation rates for the 4.72 ka IRH are shown in Figures 2 [and -](#)
 394 3. In total, these grids are made of ~89 000, 500-m spaced points, which cover an area of ~610 000
 395 km², or ~30% of the total surface area of the WAIS. The grids span most of [the](#) PIG and THW glacier
 396 catchments, as well as the Ronne (upper Rutford, Institute, and Möller) and upper western Ross
 397 (Bindschadler, Kamb, MacAyeal, and Whillans) catchments (IPY Antarctic boundaries G-H, J-Jpp,
 398 and Ep-F; Mouginot et al. (2017); Fig. 1-2). Overall, the 4.72 ka IRH is shallower within the IMIS
 399 and upper PIG and THW catchments, as well as on the Ross side of the [WD-central divide](#) where ice
 400 thickness is particularly deep (Fig. 2b). Conversely, the 4.72 ka IRH is deeper in the ice near a 400-m
 401 high bedrock plateau that separates the northern and southern basins of PIG (Vaughan et al., 2006)
 402 and at two locations in the upstream parts of the main trunk of THW where ice flows over highs in
 403 subglacial topography (Fig. 2b).

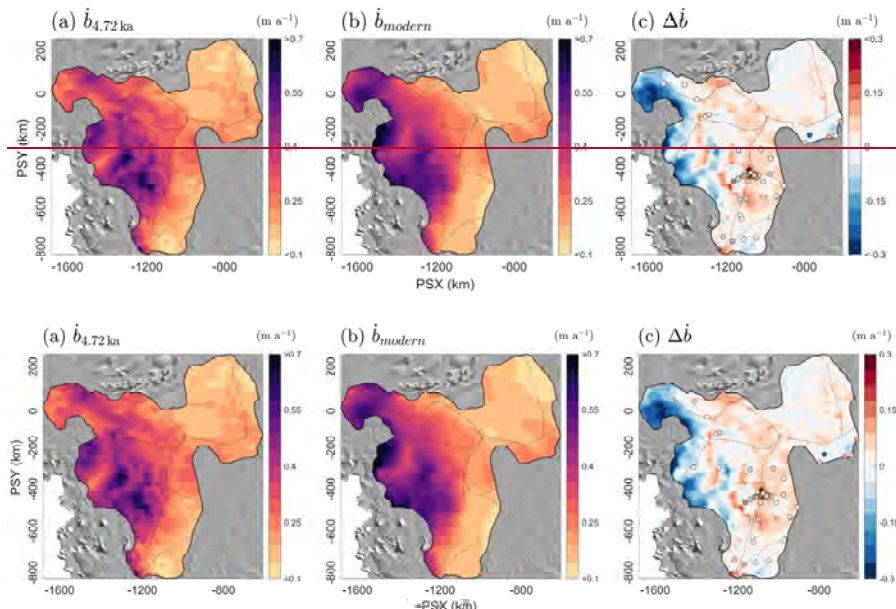


404
 405 Figure 2. Gridded depths for the 4.72 ka IRH across the model domain covering the PIG, THW, and
 406 Institute and Möller ice-stream catchments. (a) Gridded depth of the 4.72 ka IRH.
 407 (b) Normalised depth of the 4.72 ka IRH relative to ice thickness.
 408 (c) Histogram showing the distribution of values in (b) with the median (
 409 \bar{p}) and the interquartile range (i.e. 25th (Q1) and 75th (Q3) quartiles) shown as solid and dashed blue lines
 respectively. The background image is the 2014 MODIS mosaic of Antarctica (Haran et al., 2018).

410 3.1. Catchment-scale accumulation estimates

411 Figure 3 shows a comparison of the ice-equivalent accumulation rates we inferred for the 4.72
 412 ka IRH (Fig. 3a) and modern SMB estimates from RACMO2 (Fig. 3b). We observe that the IRH
 413 accumulation rate pattern for the last 4.72 ka is similar to the modern pattern of accumulation rates for
 414 the Amundsen Sea sector of the WAIS, which is dominated by higher coastal accumulation rates that
 415 progressively decrease inland [towards the ice divide](#) to reach their lowest rates over the Ross side of
 416 [the divide](#) (Fig. 3a-b). Differences in accumulation [rates](#) between the 4.72 ka-to-present estimates and
 417 modern values are mainly observed directly upstream of the main trunks of PIG and THW, where
 418 modern rates are much higher (up to 0.2 m a⁻¹ ice equivalent) than for the 4.72 ka-to-present estimates
 419 (Fig. 3c). In comparison, higher accumulation rates for the last 4.72 ka [compared relative](#) to modern

420 rates are observed for the entire stretch of the Amundsen-Weddell-Ross divide (Fig. 3c; Table 2).
 421 Noticeably over the IMIS catchment, little change is observed between the two periods. Over the
 422 entire model domain, we observe a median relative increase percentage change value of 436% in
 423 higher accumulation rates since 4.72 ka compared with modern rates (Fig. 4; Table 2); however, when
 424 considering only the values that fall within 100 km of either side of the Amundsen-Weddell-Ross
 425 divide (i.e. in the accumulation zone of the Amundsen, Weddell, and Ross Sea sectors and where
 426 mean surface speeds equal average ~ 7 m a⁻¹), we obtain a median percentage change value of 18%
 427 higher accumulation compared with modern accumulation rates (Fig. 4).



428
 429 Figure 3. Gridded estimates of ice-equivalent accumulation rates for the last 4.72 ka and modern times.
 430 (a) Gridded accumulation rates inferred from the 4.72 ka IRH. (b) Modern (1979 – 2019) modelled SMB rates
 431 from RACMO2. (c) Difference between 4.72 ka-to-present and modern accumulation rates (red = 4.72 ka-to-
 432 present accumulation higher than modern times, blue = 4.72 ka-to-present accumulation lower than modern
 433 times). The dots represent the difference between the value for the nearest grid cell in (a) and time-averaged
 434 accumulation rates at each of the 79 core locations (see Section 2.4; Fig. S6). The background image is the 2014
 435 MODIS mosaic of Antarctica (Haran et al., 2018).

436 Comparison between our 4.72 ka-to-present accumulation-rate estimates and 79 core-derived
 437 point-based accumulation measurements for modern times (1651–2010 CE) are shown in Figures 3
 438 and 3–4 and S6. This evaluation shows that the 4.72 ka-to-present accumulation-rate estimates for the
 439 nearest grid cell to each point measurement are, on average, +822% ($p < 0.0015$, $n = 79$) higher for
 440 cores situated over across the entire grid ($p < .0015$, $n = 79$) and +923% ($p < 0.0001$, $n = 59$) higher for
 441 cores found within 100 km of the divide than compared with modern accumulation rates ($p < .0001$,
 442 $n = 59$; Figs. 4 and S6). In comparison, a similar analysis between grid cells from the 4.72 ka-to-
 443 present accumulation-rate estimates and RACMO2 at these 79 core locations shows mid-Holocene
 444 accumulation rate estimates are, on average, 32% ($P < .00002$, $n = 79$) higher for cores situated
 445 across the entire grid and 36% higher for cores found within 100 km of the divide ($p < .00001$,
 446 $n = 59$; Fig. S6). This result confirms that the relative difference-change in for gridded accumulation

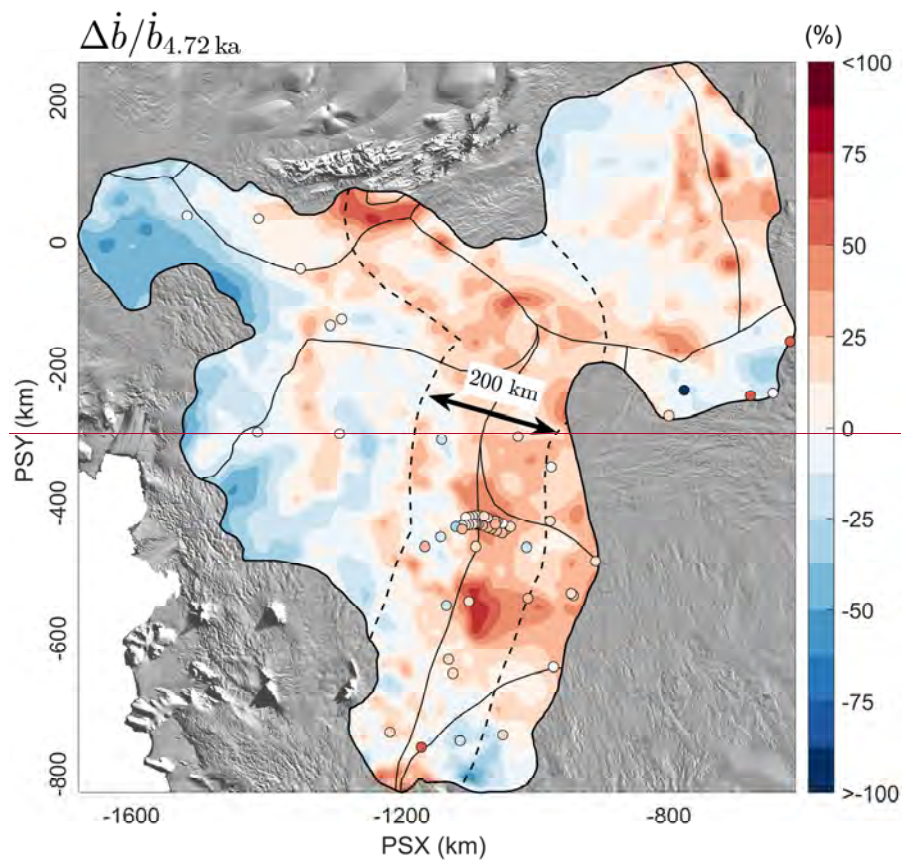
448 rates between the 4.72 ka-to-present and modern modelled accumulation rates is consistent with
449 modern rates from point-based measurements.

450 Table 2. Summary statistics for the modern (modelled and observational) and 4.72 ka-to-present ice-
451 equivalent accumulation rates at the catchment-scale and over the [Amundsen-Weddell-Ross divide](#)WD. Values
452 for the [Amundsen-Weddell-Ross divide \(abbreviated CD here\)](#)WD are for all points that fall within 100 km of
453 either side of the divide (see dashed line in Figure 4). $\tilde{\mu}$ refers to the median and IQR represents the Interquartile
454 Range calculated by computing the difference between the 75th and 25th percentiles. [Note that the values](#)
455 [provided in the text represent the median relative change from the cell-by-cell change between each grid \(Fig.](#)
456 [4\), rather than the relative change of the median values provided here.](#)

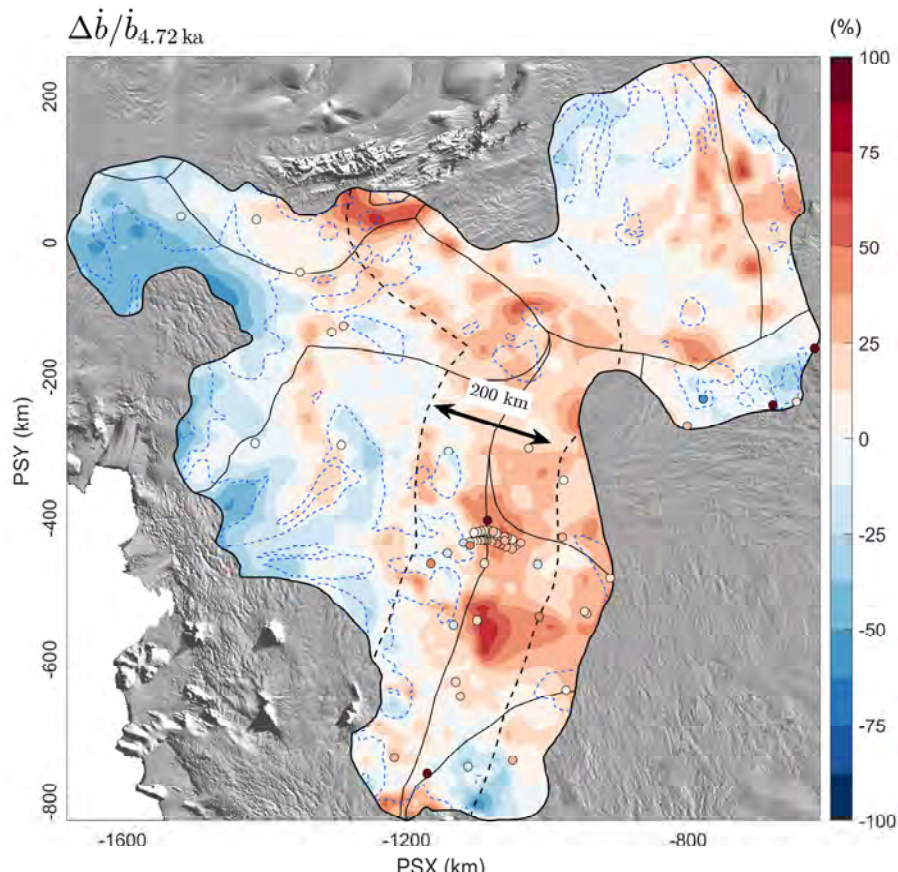
	<i>Catchment-wide</i>		<i>WD-CD only</i>	
	<i>Accumulation rate (m a⁻¹)</i>	<i>$\tilde{\mu}$</i>	<i>IQR</i>	<i>$\tilde{\mu}$</i>
<i>Modern (model)</i>	0.23	0.23		0.22
<i>Modern (cores)</i>	0.24	0.12		0.24
<i>4.72 ka-to-present</i>	0.27	0.18		0.27

457

458 For WD14 specifically, the nearest grid node to the ice core site shows a 22% higher
459 accumulation rate from 4.72 ka to present compared with modern accumulation rates (Fig. 4). There,
460 our IRH inferred accumulation rate is 0.28 ± 0.01 m a⁻¹, with the nearest IRH point situated 1.2 km
461 away from WD14 showing an accumulation rate of 0.27 ± 0.01 m a⁻¹. This is only slightly higher than
462 the direct ice core reconstruction of accumulation rates at WD14, which show up to 19% (0.25 m a⁻¹)
463 higher accumulation than modern rates (0.21 m a⁻¹) since 4700 years BP (Fudge et al., 2017).



464



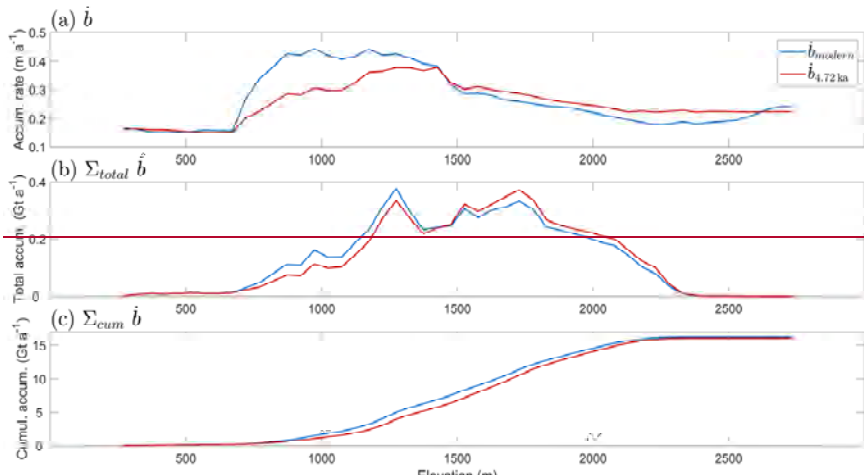
465
466 Figure 4. Relative difference-change in accumulation rates between the 4.72 ka-to-present estimates
467 and modern rates. The points on the map represent the relative difference-change in ice-equivalent accumulation
468 rate between the nearest grid cell in the 4.72 ka-to-present grid and the 79 modern observations from cores at
469 accumulation measurements from snow, firn, and ice cores (Figs. 1 and S65; see Sect. 2.4). The dashed black
470 outline line represents the 100-km boundary on either side of the Amundsen-Weddell-Ross divide used to
471 provide the summary statistics in Section 3.1 and Table 2. The dashed blue line shows the contours of the upper
472 limit of the interquartile range for the D parameter (D ≤ 0.34) (Sect. 2.2.1-2.2.2). The background image is the
473 2014 MODIS mosaic of Antarctica (Haran et al., 2018).

474 **3.2 Elevation-dependent accumulation estimates**

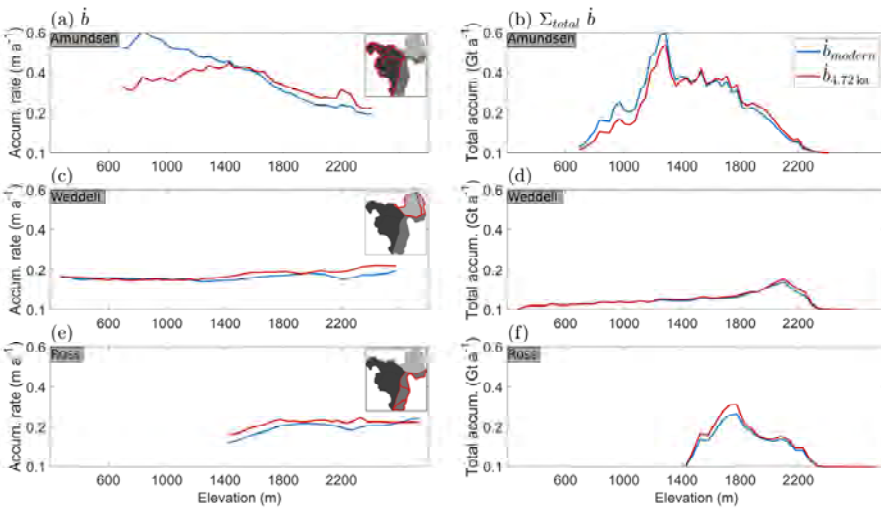
475 While Figures 3 and 4 help to assess potential differences in patterns and rates across spatial
476 scales, considering accumulation-rate differences in terms of elevation can inform how topography
477 influences accumulation and whether this has changed over time. As a result We binned the ice-
478 equivalent accumulation values for each by 50-m elevation bands across the our model domain three
479 main catchments covering our grid (Amundsen, Weddell and Ross) for both the 4.72 ka-to-present
480 estimates and modern model rates (RACMO2), and calculated the mean accumulation rate and, the
481 total accumulation rate, and the cumulative sum of total accumulation rate for each bin over the entire
482 elevation gradient of the two grids (Fig. 5). As above, wWe again find observe that the accumulation-

483 rate estimates for the period since 4.72 ka are lower at lower elevations (~700 – 1400 m) over the
 484 Amundsen sector compared with RACMO2, and but begin to exceed overtake RACMO2 near the
 485 1400-m elevation band where the 4.72 ka-to-present accumulation rate is higher than modern times
 486 across the divide up until ~24600 m in elevation (Fig. 5a-b). We also note that whilst an elevation-
 487 dependent gradient in accumulation rates, dominated by high accumulation at the coast decreasing
 488 inland, exists over this sector for the mid-Holocene, it is much less marked than for present rates. This
 489 is not surprising, as this sector is where we observe the largest relative uncertainties in inferred
 490 accumulation rates across our grid (Fig. S4), indicating that the 1-D model is less able to produce
 491 realistic accumulation rates in the downstream end of our grid where ice flow is faster and strain rates
 492 are likely higher. In comparison to the Amundsen sector, accumulation rates since 4.72 ka are
 493 generally higher at all elevations for the Weddell and Ross sectors compared with the present,
 494 although this difference is less than over the Amundsen sector (Fig. 5 c-f). The lack of a large
 495 difference between the two datasets at elevations of ~250 – 700 m is primarily dominated by
 496 accumulation rates over IMIS, which, in contrast to the PIG and THW regions, is less exposed to the
 497 large accumulation gradients characteristic of the Amundsen Sea Embayment, i.e. higher coastal
 498 accumulation decreasing inland.

499
500



← Formatted: Indent: First line: 0.63 cm



501
 502 Figure 5. Comparison of ice-equivalent accumulation rates between the 4.72 ka-to-present estimates and
 503 modern rates (RACMO2) binned for each 50-m elevation bands across our study the three main catchments
 504 considered here (Amundsen, Weddell, and Ross). (a, c, e) Mean accumulation rate averaged per 50-m elevation
 505 band across the survey-specific catchment area in m a^{-1} . (b, d, f) Total accumulation rate per 50-m elevation
 506 band across the specific catchment area in Gigatonnes Gt a^{-1} . (e) Cumulative sum of total
 507 accumulation rate per 50-m elevation band in Gt a}^{-1}.

508 **4. Discussion**

509 **4.1. Comparison with other Holocene accumulation estimates**

← Formatted: Indent: First line: 1.27 cm

510 Previous studies of past accumulation rates over the WAIS have shown that accumulation varied
 511 temporally during the Holocene. Using a single airborne RES profile over the Amundsen Sea sector,
 512 Siegert and Payne (2004) showed that accumulation rates were approximately the same at 3.1 ka
 513 compared with modern rates, but $\sim 0.3 \text{ m a}^{-1}$ greater ($\sim 15\%$) than current rates between 3.1-6.4 ka,
 514 before which accumulation was $\sim 50\%$ of modern rates between 6.4 and 16.0 ka. Similarly, Neumann
 515 et al. (2008) found that accumulation rates at the WD-central divide were $\sim 30\%$ higher between 3-5 ka
 516 than modern values based on a dense network of IRHs traced on ground-based RES data, while
 517 Karlsson et al. (2014) found that accumulation patterns had likely changed twice during the early to
 518 mid-Holocene over PIG from the lack of a model fit between the depths and ages of two prominent
 519 IRHs. Using the updated WD14 record, Fudge et al. (2016) showed that accumulation rates was were
 520 higher there in the mid to late-Holocene (19% between 4.72 ka BP and the present), a trend that was
 521 also observed by Koutnik et al. (2016), who found a 20% increase in accumulation rates between 2-4
 522 ka compared with modern rates from a ground-based RES profile across the ice divide.

523 These studies together point to a period of increasing accumulation observed at the WD14 Ice
 524 Core from ~ 7 ka onwards (Fudge et al., 2016; their Figure 2), with its peak matching the age of the
 525 4.72 ka IRH used here. Thus, our accumulation-rate estimates likely form part of a wider pattern of a
 526 sustained increase in accumulation across the Amundsen-Weddell-Ross divideWD over several
 527 millennia. In showing that mean accumulation rates since 4.72 ka were 18% greater than modern rates
 528 modelled from RACMO2 across the Amundsen-Weddell-Ross divideWD, our results provide a much
 529 wider regional picture-support for the hypothesis (across $\sim 30\%$ of the WAIS) that accumulation rates
 530 during the mid-Holocene exceeded modern rates over-across large parts of central West Antarctica.

531 We gain confidence in the ability of the Nye model to estimate past accumulation rates from the
532 4.72 ka IRH, given that its outputs match relatively well with the direct reconstruction of mean
533 accumulation rates at the WD14 Ice Core, with values at the ice core of $0.27 \pm 0.01 \text{ m a}^{-1}$ (this study)
534 compared with 0.25 m a^{-1} for Fudge et al. (2016). This also suggests that the WD14 Ice Core suitably
535 represents atmospheric conditions across the wider WD. A possible explanation for the higher
536 accumulation rates this pattern during the mid-Holocene compared with modern values is that they
537 represent a continued climatic transition from the LGM (Steig et al., 2001). Alternatively, it has been
538 suggested that seasonal or interannual variability, such as a weaker circumpolar vortex (van Den
539 Broeke and van Lipzig, 2004; Neumann et al., 2008), or teleconnections to tropical Pacific Ocean
540 warming (Sproson et al., 2022), may also lead to such difference. We did not find evidence for
541 significant changes in accumulation patterns between the mid-Holocene and modern times, suggesting
542 that the current spatial pattern of high accumulation ~~at the on the Amundsen side of the divide coast~~
543 ~~transitioning to, decreasing low accumulation inland towards at the divide on the Ross side of the~~
544 ~~divide was~~ stable throughout the mid-Holocene over PIG and THW, as previously suggested by others
545 (Siegert and Payne, 2004; Neumann et al., 2008; Koutnik et al., 2016).

546 We also find that ~~a~~Accumulation estimates for the 4.72 ka-to-present are smaller than modern
547 rates in the lowest elevation bands (~~i.e.~~ $<1400 \text{ m}$), ~~particularly over, particularly over the Amundsen~~
548 ~~Sector~~ (Figs. 4, 5 a-d). This pattern was also ~~reported~~ found by Medley et al. (2014), who compared
549 modern observational and modelled data ~~within~~ over this sector ~~in ASE~~ and hypothesised that this
550 discrepancy at low elevations resulted primarily from a lack of sufficient accumulation measurements
551 in the lower sections of their survey area. In our case, these low-elevation values are close to the
552 boundary where we consider the LLA acceptable for the 4.72 ka IRH, albeit where D values are
553 higher than for the rest of the catchment (Figure S1d), so it is more likely that accumulation rates
554 calculated there are affected by ice-flow gradients and their influence upon IRH depths ~~leading to~~
555 ~~lower accumulation rates there~~. Despite this caveat, Figures 5b and 5d shows that values at low
556 elevations (250 – 1200 m) contribute relatively little to the total accumulation (by mass) over our
557 survey area.

558 We suggest that future ice-sheet modelling studies investigate the difference in accumulation rates
559 inferred from our 1-D model using multi-dimensional flowband models to assess effects of divergent
560 and convergent flow on IRH depth and ultimately accumulation rates, as previously considered
561 elsewhere in Antarctica (MacGregor et al., 2009). This could be conducted along a flowline
562 transitioning from the slow-flowing regions directly downstream of the Amundsen-Weddell-Ross
563 divide ~~WD~~ to the coastal margins of our grid, particularly over THW where we observe the largest
564 uncertainties in accumulation rates. In addition, we suggest that future modelling studies use the
565 accumulation-rate variability from the WD14 Ice Core as a climate forcing in their ice-sheet models.
566 Koutnik et al. (2016) previously showed that the WD14 record is unique in that it provides a reliable
567 record of accumulation-rate variability during the Holocene, which other East Antarctic ice-core
568 records often used to reconstruct the evolution of the WAIS do not possess. We found that these
569 higher accumulation rates are spatially extensive across nearly one third of the WAIS, further
570 suggesting that the WD14 Ice Core is indeed representative of the wider WAIS and can be used in
571 regional or continental ice-sheet models as a reliable climate forcing for the region. Future regional
572 and continental ice-sheet models should make use of this record to adjust their climatic boundary
573 conditions to provide improved estimates of ice-elevation change and grounding-line evolution over
574 Antarctica.

575 4.2 Impact for ice-sheet elevation change during the Holocene

576 Our results reinforce the evidence that accumulation rates have varied temporally across West
577 Antarctica during the Holocene, a finding that must be considered by future modelling studies that
578 simulate past sea-level rise from Antarctica since the LGM. Model results from Steig et al. (2001)

← - - Formatted: Indent: First line: 1.27 cm

579 suggest that the maximum elevation of the WAIS was most likely reached during the early to mid-
580 Holocene (around ~7 ka) following higher accumulation rates at the late glacial-interglacial
581 transition, after which ~~elevations the WAIS~~ slowly declined to present conditions as the sea-level-rise-
582 induced kinematic wave reached the ice-sheet interior and outpaced the increase in accumulation
583 rates. However, ~~a moderate mid Holocene increase in accumulation rates~~higher accumulation rates in
584 the mid-Holocene relative to the present, which our results suggest occurred widely spatially across
585 the WAIS, would, ~~if sustained,~~ likely delay the timing of ~~theis thinning decline in elevation~~ by
586 several thousand years (Steig et al., 2011).

587 Using a flowband model, Koutnik et al. (2016) suggested that ~~the an~~ increase of up to 40% in
588 accumulation rates for the period 9 – 2 ka would likely ~~have lead~~ to an increase in ice thickness of
589 tens of metres~~s~~ during the mid-Holocene. Although this finding was warranted by physical
590 assumptions around the response time of the ice-sheet interior to adjust to an increase in accumulation
591 in the model, it points to the potential for the divide to have thickened by several metres over a
592 relatively short period of time from increased accumulation rates alone. However This noted, because
593 Because the WAIS is also sensitive to ice-dynamical changes at the ice-sheet margins (e.g. grounding
594 lineGL retreat and/or calving), an increase in accumulation rates in the upper part of the ice sheet may
595 not necessarily result in enough thickening to counteract potential dynamical losses from ice
596 dynamics further downstream (Jones et al., 2022). Conway and Rasmussen (2008) reported that the
597 WAIS Amundsen-Ross Divide is currently thinning and migrating towards the Ross Sea at a speed of 10
598 m a⁻¹, but they were unable to determine whether this was in response to long-term (last two
599 millennia) accumulation-rate changes there or short-term (last few centuries) ice-dynamical forcing
600 from the coastal margins of the Amundsen and Ross sectors. More recently, Balco et al. (2023)
601 showed that Thwaites and Pope glaciers experienced 35 m of thickening in the mid-to-late Holocene,
602 when accumulation rates were higher than present. While this thickening relative to present was
603 attributed to glacio-isostatic rebound, it is also possible that higher accumulation rates in the upstream
604 sections of the WAIS contributed to this thickening, if sustained over millennia.

605 The lack of an ice-dynamical component in the model used here precludes us from ~~reaching~~ ← - - - Formatted: Indent: First line: 1.27 cm
606 ~~evaluating any ice-surface-elevation change associated with changes such a conclusion; however,~~
607 ~~higher~~ accumulation rates. However, of up to at least 18% higher accumulation rates during the mid-
608 Holocene relative to the present across 30% of the WAIS ~~could likely~~ be consistent with an
609 elevation increase of several tens of metres~~s~~ in ice thickness, according to Koutnik et al. (2016) e.g.
610 Figure 10 of Koutnik et al., 2016. Even if tens of metres of ice-surface-elevation change occurred, it
611 This potential increase in surface elevation is still unlikely to significantly affect the steady-state
612 assumption of the 1-D model used here (constant ice thickness over time), because such considering
613 that these changes are small (a few per cent of the ice thickness) and that ice thickness exceeds 3500
614 m in places over our survey area.

615 We encourage future ice sheet models to test a range of scenarios that would account for variable
616 accumulation rates between the LGM and the present over the WAIS by using the WD14
617 reconstructed accumulation rates from Fudge et al. (2016) as a guide, which, as we show here,
618 suitably represents the pattern of accumulation variability over both time and space in West
619 Antarctica.

620 4.3 Impact for grounding-line evolution during the Holocene over the WAIS ← - - - Formatted: Indent: First line: 1.27 cm

621 Finally, we may also consider the possibility for Holocene ice thickening at the divide from
622 increased accumulation rates to affect downstream grounding-lineGL evolution over the WAIS.
623 Recent evidence from ice-sheet modelling and field measurements suggests that grounding-lineGL
624 retreat during the Holocene was not monotonic, particularly at the Ross and Weddell Sea sides of the
625 WAIS (Bradley et al., 2015; Kingslake et al., 2018; Neuhaus et al., 2021). Rather, Kingslake et al.
626 (2018) showed that the grounding-lineGL position in the Ross and Weddell Sea sectors initially

627 retreated from the LGM inland until ~~~10.2 – 9.7~~ ~~9.7~~ – 10.2 ka, and then re-advanced to its modern
628 position sometime during the Holocene. Although they attributed this change in grounding-lineGL
629 position to the solid Earth viscoelastic response due to ice-sheet mass change and the subsequent re-
630 grounding around pinning points, it has also been suggested that an increase in accumulation rates
631 upstream of the grounding lineGL could lead to a re-advance via ice thickening there and a
632 subsequent increase in ice flow (Steig et al., 2001; Koutnik et al., 2016; Jones et al., 2022). Across
633 parts of the Weddell Sea Embayment, several studies (Ross et al., 2011; Hein et al., 2016; Ashmore et
634 al., 2020a) have produced evidence for stability of the LGM ice thickness there until the early to mid-
635 Holocene (Ross et al., 2011; Hein et al., 2016; Ashmore et al., 2020a), contrary to most of the WAIS,
636 after which abrupt thinning of ~400 m contributed ~1.4 – 2 m of sea level rise (Hein et al., 2016). A
637 possible explanation for this delayed thinning in the Weddell Sea Embayment is that increased
638 snowfall in the upper WAIS might have counteracted ice-dynamical processes at the coast until the
639 mid-to-late Holocene (Hein et al., 2016; Spector et al., 2019). Similarly, over part of the Ross Sea
640 sector, Neuhaus et al. (2021) showed that the grounding lineGL over Whillans, Kamb, and
641 Bindschadler ice streams retreated to its minimum Holocene position in the mid to late-Holocene, and
642 then re-advanced between ~~2 – 1.4 – 2~~ ka, coinciding with periods of warmer and colder climates,
643 respectively. They concluded that the reported grounding-lineGL migration was likely dominated by
644 modest climate-induced changes upstream rather than ice dynamics further downstream, as suggested
645 for the Weddell Sea sector (Hein et al., 2016).

646 Our results, which provide strong and widespread evidence for higher accumulation along the
647 Amundsen-Weddell-Ross divide during the mid-Holocene compared with the present, support these
648 hypotheses further, as higher accumulation rates at the divide would likely result in upstream
649 thickening (Sect. 4.2). In the absence of ice-dynamical processes counter-balancing this increase in
650 accumulation rates, the grounding-line should advance in these regions. However, we note that the
651 pattern of grounding-line retreat and readvance has not been observed over the Amundsen Sea sector
652 (Kingslake et al., 2018; Johnson et al., 2020; 2021; Braddock et al., 2022) despite the accumulation-
653 rate increase we also observed along the Amundsen-Weddell-Ross divide and the recent results from
654 Balco et al. (2023). This complication may indicate that the Amundsen sector is more strongly
655 influenced by coastal changes in ice dynamics, for which even moderate changes in accumulation rate
656 cannot compensate.

657 5. Conclusion

658 Using a ubiquitous ~~i~~Internal ~~r~~Reflecting ~~h~~Horizon found across most of the Pine Island, Thwaites,
659 and Institute and Möller ice-stream catchments, we have estimated mid-Holocene accumulation rates
660 in the relatively slow-flowing parts of West Antarctica, (representing 30% of total surface area of the
661 WAIS) using a 1-D ice-flow model.

662 By comparing our Holocene accumulation-rate estimates with a modern climate reanalysis
663 models and observational syntheses, we estimated that accumulation rates across the Amundsen-
664 Weddell-Ross Sea divide since 4.72 ka were, on average, 18% higher than modern ~~accumulation~~
665 ~~rates values~~. While the accumulation rates have therefore varied temporally, Our results suggest that
666 spatial patterns of accumulation ~~between regions across the~~ across the WAIS have remained ~~similar~~
667 ~~stable~~ during this period, i.e., higher accumulation rates ~~on the Amundsen side of the divide at the~~
668 ~~coast and transitioning to~~ lower accumulation rates ~~at the ice on the Ross side of the divides~~. The
669 higher accumulation ~~rates estimates~~ reported here for the mid-Holocene compared to the present agree
670 well with ~~previous~~ ~~earlier~~, ~~more~~ spatially-focused studies of accumulation rates ~~across the WAIS, all~~
671 ~~of which which all~~ indicate higher accumulation rates ~~of between (+15 and - 30%)~~ over the ~~past~~ ~5
672 ka ~~compared with the present~~. This change in magnitude occurred at a time of asynchronous
673 grounding-line migration over the WAIS, including re-advances of the grounding line in the Weddell
674 and Ross sectors and evidence for delayed deglaciation in the Weddell Sea side of the WAIS.

← - - -
Formatted: List Paragraph, Numbered + Level: 1 +
Numbering Style: 1, 2, 3, ... + Start at: 1 + Alignment:
Left + Aligned at: 0.63 cm + Indent at: 1.27 cm

675 Finally, our results further support the use of the WAIS Divide ice-core record to assess past
676 atmospheric conditions across the wider Western Divide and even a substantial portion of the WAIS,
677 making it a powerful dataset for ice-sheet models. The higher mid-Holocene accumulation estimates
678 compared to modern reported inferred here over large sectors of the WAIS occurred at a time of
679 sustained, millennial-scale increase in accumulation rates found at the WAIS Divide Ice Core. This
680 pattern indicates that the ice core is suitably representative of the climatic conditions of the wider
681 region over time. We suggest that future regional or continental ice-sheet modelling studies base their
682 palaeoclimate forcing on modern spatial SMB products that are modulated over time using the WAIS
683 Divide Ice Core record. This will enable those models to obtain a more realistic climatic forcing
684 representative of the past conditions of the wider WAIS, and ultimately, constrain ice-sheet volume
685 change and grounding-line evolution during the Holocene. The higher accumulation rates reported
686 here occurred at a time of asynchronous grounding line migration over the WAIS, including re-
687 advances of the grounding line in the Weddell and Ross sectors and evidence for delayed deglaciation
688 in the Weddell Sea side of the WAIS. We suggest that ice sheet model account for the evolution of
689 accumulation rates over time when predicting past and future sea level coming from West Antarctica
690 instead of using a fixed Last Glacial Maximum value.

691 **Code availability**

692 All the codes used to produce the results presented in this paper will be made available on the
693 GitHub page of Julien A. Bodart (<https://github.com/julbod>, last accessed: 15 October 2022) and on
694 Zenodo (Bodart *et al.*, 2023a) upon acceptance of this manuscript.

695 **Data availability**

696 The IRH information for each of the three surveys used in this paper are archived in open-
697 access repositories (Ashmore *et al.*, 2020b; Bodart *et al.*, 2021b; UTIG R1 layer to be made available
698 via USAP-DC *in due course*) with references and links provided in the reference list. The BAS
699 airborne radar data which were used to extract the IRHs used in this paper are fully available at the
700 UK Polar Data Centre via the Polar Airborne Geophysics Data Portal (see Fremand, Bodart *et al.*,
701 2022). The full-RACMO-2.3p2 product is available on request from j.m.vanwessem@uu.nl or
702 m.r.vandenbroeke@uu.nl. Links to access the observational point-based datasets used here are
703 available from the respective references mentioned in the text (Section 2.4). The gridded depth and
704 accumulation output from this study will be archived on Zenodo at the UK Polar Data Centre upon
705 acceptance of this manuscript (Bodart *et al.*, 2023b).

706 **Author contribution**

707 J.A.B. designed the study with supervision from R.G.B., D.A.Y., and D.D.B. J.A.B
708 performed the data processing, gridding, and 1-D modelling, with contributions from J.A.M. for the
709 modelling approach. J.A.B. interpreted the results with input from R.G.B., D.A.Y., D.D.B., and
710 J.A.M. J.A.B. wrote the paper, with edits from [R.G.B., D.A.Y., J.A.M., D.W.A., E.Q., A.S.H.,](#)
711 [D.G.V., D.D.B.all co-authors.](#)

712 **Competing interests**

713 The authors declare that they have no conflict of interest.

714 **Acknowledgments**

715 The authors would like to dedicate this work to our dear friend and colleague, Professor
716 [David Vaughan, who recently passed away.](#) This study was motivated by the AntArchitecture SCAR
717 Action Group. UTIG acknowledges the high school students who did the original AGASEA layer
718 interpretation.

719 **Financial support**

720 J.A.B. was supported by the NERC Doctoral Training Partnership grant (NE/L002558/1),
721 hosted in the Edinburgh E³ DTP [programme](#)[program](#). J.A.B. also acknowledges the Scottish Alliance
722 for Geoscience, Environment and Society (SAGES) for funding a Postdoctoral and Early Career
723 Researcher Exchanges scheme to UTIG. Support for UTIG data analysis was received from NSF
724 grant nos CDI-0941678, PLR-1443690, and PLR-10437661, as well as the G. Unger Vetlesen
725 Foundation and the UTIG Gale White and Ewing/Worzel Fellowships. This is UTIG contribution
726 number: xxxx (TBD).

727 **References**

728 Arndt, J.E., Hillenbrand, C.D., Grobe, H., Kuhn, G. and Wacker, L.: Evidence for a dynamic
729 grounding line in outer Filchner Trough, Antarctica, until the early Holocene, *Geology*, 45(11), 1035-
730 1038, <https://doi.org/10.1130/G39398.1>, 2017.

731 Ashmore, D.W., Bingham, R.G., Ross, N., Siegert, M.J., Jordan, T.A. and Mair, D.W.:
732 Englacial architecture and age-depth constraints across the West Antarctic Ice Sheet, *Geophys. Res.
733 Lett.*, 47 (6), p.e2019GL086663, <https://doi.org/10.1029/2019GL086663>, 2020a.

734 Ashmore, D.W., Bingham, R.G., Ross, N., Siegert, M., Jordan, T.A. and Mair, D.W.F.:
735 Radiostratigraphy of the Weddell Sea sector of West Antarctica, v2.0.0, Zenodo [data set],
736 <https://doi.org/10.5281/zenodo.4945301>, 2020b.

737 [Balco, G., Brown, N., Nichols, K., Venturelli, R.A., Adams, J., Braddock, S., Campbell, S.,
738 Goehring, B., Johnson, J.S., Rood, D.H. and Wilcken, K.: Reversible ice sheet thinning in the
739 Amundsen Sea Embayment during the Late Holocene, *The Cryosphere Discussions*, pp.1-24,
740 https://doi.org/10.5194/tc-2022-172](#), 2022.

741 Beem, L.H., Young, D.A., Greenbaum, J.S., Blankenship, D.D., Cavitte, M.G., Guo, J. and
742 Bo, S.: Aerogeophysical characterization of Titan Dome, East Antarctica, and potential as an ice core
743 target, *The Cryosphere*, 15 (4), 1719-1730, <https://doi.org/10.5194/tc-15-1719-2021>, 2021.

744 Bingham, R.G. and Siegert, M.J.: Radio-echo sounding over polar ice masses. *J Environ. Eng.
745 Geoph.*, 12 (1), <https://doi.org/10.2113/JEEG12.1.47>, 47-62, 2007.

746 Bracegirdle, T.J., Colleoni, F., Abram, N.J., Bertler, N.A., Dixon, D.A., England, M., Favier,
747 V., Fogwill, C.J., Fyfe, J.C., Goodwin, I. and Goosse, H.: Back to the future: Using long-term
748 observational and palaeo-proxy reconstructions to improve model projections of Antarctic climate,
749 *Geosci. J.*, 9 (6), 255, <https://doi.org/10.3390/geosciences9060255>, 2019.

750 Braddock, S., Hall, B.L., Johnson, J.S., Balco, G., Spoth, M., Whitehouse, P.L., Campbell, S.,
751 Goehring, B.M., Rood, D.H. and Woodward, J.: Relative sea-level data preclude major late Holocene
752 ice-mass change in Pine Island Bay, *Nat. Geosci.*, 15, 568-572, [https://doi.org/10.1038/s41561-022-00961-y](https://doi.org/10.1038/s41561-022-
753 00961-y), 2022.

754 Bradley, S.L., Hindmarsh, R.C., Whitehouse, P.L., Bentley, M.J. and King, M.A.: Low post-
755 glacial rebound rates in the Weddell Sea due to Late Holocene ice-sheet readvance, *Earth Planet. Sc.
756 Lett.*, 413, 79-89, <https://doi.org/10.1016/j.epsl.2014.12.039>, 2015.

757 Bodart, J. A., Bingham, R. G., Ashmore, D. W., Karlsson, N.B., Hein, A. S., and Vaughan, D.
758 G.: Age-depth stratigraphy of Pine Island Glacier inferred from airborne radar and ice core
759 chronology, *J. Geophys. Res.-Earth*, 126, e2020JF005927, <https://doi.org/10.1029/2020JF005927>,
760 2021a.

761 Bodart, J.A., Bingham, R.G., Ashmore, D.W., Karlsson, N.B., Hein, A.S., and Vaughan,
762 D.G.: Dated radar stratigraphy of the Pine Island Glacier catchment (West Antarctica) derived from
763 BBAS-PASIN (2004-05) and OIB-MCoRDS2 (2016/2018) surveys, v.1.0.0, UK Polar Data Centre,
764 Natural Environment Research Council, UK Research and Innovation [data set],
765 <https://doi.org/10.5285/F2DE31AF-9F83-44F8-9584-F0190A2CC3EB>, 2021b.

766 [Bodart, J.A.: Calculate WAIS Holocene accumulation from airborne radar reflector, v.1.0.0.,](#)
767 [Zenodo \[code\], doi TBD, 2023a.](#)

768 Bodart, J.A., Bingham, R.G., Young, D.A., MacGregor, J.M., Ashmore, D.W., Quartini, E.,
769 Vaughan, D.G., and Blankenship D.D.: Gridded [depth and accumulation-and depth](#) products from
770 dated airborne radar stratigraphy over West Antarctica during the mid-Holocene, v.1.0.0, [UK-Polar](#)
771 [Data Centre, Natural Environment Research Council, UK Research and Innovation](#)[Zenodo](#) [data set],
772 doi TBD, 2023b.

773 Buizert, C., Fudge, T.J., Roberts, W.H., Steig, E.J., Sherriff-Tadano, S., Ritz, C., Lefebvre, E.,
774 Edwards, J., Kawamura, K., Oyabu, I. and Motoyama, H.: Antarctic surface temperature and elevation
775 during the Last Glacial Maximum, *Science*, 372 (6546), 1097-1101,
776 <https://doi.org/10.1126/science.abd2897>, 2021.

777 Burgener, L., Rupper, S., Koenig, L., Forster, R., Christensen, W.F., Williams, J., Koutnik,
778 M., Miege, C., Steig, E.J., Tingey, D. and Keeler, D.: An observed negative trend in West Antarctic
779 accumulation rates from 1975 to 2010: Evidence from new observed and simulated records. *J.*
780 *Geophys. Res.-Atmos.*, 118 (10), 4205-4216, <https://doi.org/10.1002/jgrd.50362>, 2013.

781 Cavitte, M.G., Blankenship, D.D., Young, D.A., Schroeder, D.M., Parrenin, F., Lemeur, E.,
782 Macgregor, J.A. and Siegert, M.J.: Deep radiostratigraphy of the East Antarctic plateau: connecting
783 the Dome C and Vostok ice core sites, *J. Glaciol.*, 62 (232), 323-334,
784 <https://doi.org/10.1017/jog.2016.11>, 2016.

785 [Cavitte, M.G., Parrenin, F., Ritz, C., Young, D.A., Liefferinge, B., Blankenship, D.D.,](#)
786 [Frezzotti, M. and Roberts, J.: Accumulation patterns around Dome C, East Antarctica, in the last 73](#)
787 [kyr, The Cryosphere, 12, pp.1401-1414. doi: 10.5194/tc-12-1401-2018, 2018.](#)

788 [Cavitte, M.G., Goosse, H., Wauthy, S., Kausch, T., Tison, J.L., Van Liefferinge, B., Pattyn,](#)
789 [F., Lenaerts, J.T. and Claeys, P.: From ice core to ground-penetrating radar: representativeness of](#)
790 [SMB at three ice rises along the Princess Ragnhild Coast, East Antarctica, J. Glaciol.](#), 68(272),
791 [pp.1221-1233, https://doi.org/10.1017/jog.2022.39, 2022.](#)

792 Chavaillaz, Y., Codron, F. and Kageyama, M.: Southern westerlies in LGM and future
793 (RCP4.5) climates, *Clim. Past*, 9 (2), 517-524, <https://doi.org/10.5194/cp-9-517-2013>, 2013.

794 Cuffey, K.M., Clow, G.D., Steig, E.J., Buizert, C., Fudge, T.J., Koutnik, M., Waddington,
795 E.D., Alley, R.B. and Severinghaus, J.P.: Deglacial temperature history of West Antarctica, *P. Natl.*
796 *A. Sci.*, 113 (50), 14249-14254, <https://doi.org/10.1073/pnas.1609132113>, 2016.

797 Cole-Dai, J., Ferris, D.G., Kennedy, J.A., Sigl, M., McConnell, J.R., Fudge, T.J., Geng, L.,
798 Maselli, O.J., Taylor, K.C. and Souney, J.M.: Comprehensive record of volcanic eruptions in the
799 Holocene (11,000 years) from the WAIS Divide, Antarctica ice core, *J. Geophys. Res.-Atmos.*, 126
800 (7), p.e2020JD032855, <https://doi.org/10.1029/2020JD032855>, 2021.

801 Corr, H.F., Ferraccioli, F., Frearson, N., Jordan, T., Robinson, C., Armadillo, E., Caneva, G.,
802 Bozzo, E. and Tabacco, I.: Airborne radio-echo sounding of the Wilkes Subglacial Basin, the
803 Transantarctic Mountains and the Dome C region, *Terra Ant. Rep.*, 13, pp.55-63.
804 <https://nora.nerc.ac.uk/id/eprint/13578> (last access: 15 October 2022), 2007.

805 CReSIS: CReSIS Radar Depth Sounder Data, Lawrence, Kansas, USA. Digital Media.
806 <http://data.cresis.ku.edu/> (last access: 15 October 2022), 2018.

807 Dansgaard, W. and Johnsen, S. J.: A flow model and a time scale for the ice core from Camp
808 Century, *Greenland, J. Glacio.*, 8 (53), 215–223, <https://doi.org/10.3189/S0022143000031208>, 1969.

809 Dattler, M.E., Lenaerts, J.T. and Medley, B.: Significant spatial variability in radar-derived
810 west Antarctic accumulation linked to surface winds and topography, *Geophys. Res. Lett.*, 46(22),
811 pp.13126-13134, <https://doi.org/10.1029/2019GL085363>, 2019.

812 DeConto, R.M. and Pollard, D.: Contribution of Antarctica to past and future sea-level rise,
813 Nature, 531 (7596), 591-597, <https://doi.org/10.1038/nature17145>, 2016.

814 Denton, G.H. and Hughes, T.J.: Reconstructing the Antarctic ice sheet at the Last Glacial
815 Maximum, *Quaternary Sci. Rev.*, 21 (1-3), 193-202, [https://doi.org/10.1016/S0277-3791\(01\)00090-7](https://doi.org/10.1016/S0277-3791(01)00090-7),
816 2002.

817 Fahnestock, M., Abdalati, W., Joughin, I., Brozena, J. and Gogineni, P.: High geoSthermal
818 heat flow, basal melt, and the origin of rapid ice flow in central Greenland, *Science*, 294 (5550),
819 2338-2342, <https://doi.org/10.1126/science.1065370>, 2001a.

820 Fahnestock, M., Abdalati, W., Luo, S. and Gogineni, S.: Internal layer tracing and age-depth-
821 accumulation relationships for the northern Greenland ice sheet, *J. Geophys. Res.-Atmos.*, 106(D24),
822 pp.33789-33797, <https://doi.org/10.1029/2001JD900200>, 2001b.

823 Favier, V., Agosta, C., Parouty, S., Durand, G., Delaygue, G., Gallée, H., Drouet, A.-S.,
824 Trouvilliez, A., and Krinner, G.: An updated and quality controlled surface mass balance dataset for
825 Antarctica, *The Cryosphere*, 7, 583-597, <https://doi.org/10.5194/tc-7-583-2013>, 2013.

826 Frémand, A.C., Bodart, J.A., Jordan, T.A., Ferraccioli, F., Robinson, C., Corr, H.F., Peat,
827 H.J., Bingham, R.G. and Vaughan, D.G.: British Antarctic Survey's Aerogeophysical Data: Releasing
828 25 Years of Airborne Gravity, Magnetic, and Radar Datasets over Antarctica, *Earth Syst. Sci. Data*,
829 14, 3379–3410, <https://doi.org/10.5194/essd-14-3379-2022>, 2022.

830 Fudge, T.J., Markle, B.R., Cuffey, K.M., Buizert, C., Taylor, K.C., Steig, E.J., Waddington,
831 E.D., Conway, H. and Koutnik, M.: Variable relationship between accumulation and temperature in
832 West Antarctica for the past 31,000 years, *Geophys. Res. Lett.*, 43(8), 3795-3803,
833 <https://doi.org/10.1002/2016GL068356>, 2016.

834 Fudge, T. J., Buizert, C., Conway, H., and Waddington, E. D.: Accumulation Rates from the
835 WAIS Divide Ice Core, v.1.0.0., U.S. Antarctic Program Data Center [data set],
836 <https://doi.org/10.15784/601004>, 2017.

837 Golledge, N.R., Fogwill, C.J., Mackintosh, A.N. and Buckley, K.M.: Dynamics of the last
838 glacial maximum Antarctic ice-sheet and its response to ocean forcing, *P. Natl. Acad. Sci.*, 109(40),
839 pp.16052-16056, <https://doi.org/10.1073/pnas.1205385109>, 2012.

840 Golledge, N.R., Levy, R.H., McKay, R.M., Fogwill, C.J., White, D.A., Graham, A.G., Smith,
841 J.A., Hillenbrand, C.D., Licht, K.J., Denton, G.H. and Ackert Jr, R.P.: Glaciology and geological
842 signature of the Last Glacial Maximum Antarctic ice sheet, *Quaternary Sci. Rev.*, 78, pp.225-247,
843 <https://doi.org/10.1016/j.quascirev.2013.08.011>, 2013

844 Haran, T., M. Klinger, J. Bohlander, M. Fahnestock, T. Painter, and T. Scambos: MEaSUREs
845 MODIS Mosaic of Antarctica 2013-2014 (MOA2014) Image Map, v.1.0.0., NASA National Snow
846 and Ice Data Center Distributed Active Archive Center [data set],
847 <https://doi.org/10.5067/RNF17BP824UM>, 2018.

848 Harrison, C. H.: Radio Echo Sounding of Horizontal Layers in Ice, *J. Glaciol.*, 12, 66, 383–
849 397, <https://doi.org/10.3189/S0022143000031804>, 1973.

850 Hein, A.S., Marrero, S.M., Woodward, J., Dunning, S.A., Winter, K., Westoby, M.J.,
851 Freeman, S.P., Shanks, R.P. and Sugden, D.E.: Mid-Holocene pulse of thinning in the Weddell Sea
852 sector of the West Antarctic ice sheet, *Nat. Commun.*, 7 (1), 1–8,
853 <https://doi.org/10.1038/ncomms12511>, 2016.

854 Hillenbrand, C.D., Kuhn, G., Smith, J.A., Gohl, K., Graham, A.G., Larter, R.D., Klages, J.P.,
855 Downey, R., Moreton, S.G., Forwick, M. and Vaughan, D.G.: Grounding-line retreat of the west
856 Antarctic ice sheet from inner Pine island Bay, *Geology*, 41 (1), 35–38,
857 <https://doi.org/10.1130/G33469.1>, 2013.

858 Hillenbrand, C.D., Bentley, M.J., Stolldorf, T.D., Hein, A.S., Kuhn, G., Graham, A.G.,
859 Fogwill, C.J., Kristoffersen, Y., Smith, J.A., Anderson, J.B. and Larter, R.D.: Reconstruction of
860 changes in the Weddell Sea sector of the Antarctic Ice Sheet since the Last Glacial Maximum,
861 *Quaternary Sci. Rev.*, 100, 111–136, <https://doi.org/10.1016/j.quascirev.2013.07.020>, 2014.

862 Hillenbrand, C.D., Smith, J.A., Hodell, D.A., Greaves, M., Poole, C.R., Kender, S., Williams,
863 M., Andersen, T.J., Jernas, P.E., Elderfield, H. and Klages, J.P.: West Antarctic Ice Sheet retreat
864 driven by Holocene warm water incursions, *Nature*, 547 (7661), 43–48,
865 <https://doi.org/10.1038/nature22995>, 2017.

866 Holschuh, N., Parizek, B.R., Alley, R.B. and Anandakrishnan, S.: Decoding ice sheet
867 behavior using englacial layer slopes, *Geophys. Res. Lett.*, 44(11), pp.5561–5570,
868 <https://doi.org/10.1002/2017GL073417>, 2017.

869 Holt, J. W., Blankenship, D. D., Morse, D. L., Young, D. A., Peters, M. E., Kempf, S. D.,
870 Richter, T. G., Vaughan, D. G., and Corr, H. F.: New boundary conditions for the West Antarctic Ice
871 Sheet: Subglacial topography of the Thwaites and Smith glacier catchments, *Geophys. Res. Lett.*, 33,
872 L09502, <https://doi.org/10.1029/2005GL025561>, 2006.

873 IPCC: Climate Change 2021: The Physical Science Basis. Contribution of Working Group I
874 to the Sixth Assessment Report of the Intergovernmental Panel on Climate Change, edited by:
875 Masson-Delmotte, V., Zhai, P., Pirani, A., Connors, S. L., Péan, C., Berger, S., Caud, N., Chen, Y.,
876 Goldfarb, L., Gomis, M. I., Huang, M., Leitzell, K., Lonnoy, E., Matthews, J. B. R., Maycock, T. K.,
877 Waterfield, T., Yelekçi, O., Yu, R., and Zhou B., Cambridge University Press, Cambridge, United
878 Kingdom and New York, NY, USA, 147–286, <https://doi.org/10.1017/9781009157896.003>, in press,
879 2021.

880 Jacobel, R. W., and Welch, B. C.: A time marker at 17.5 kyr BP detected throughout West
881 Antarctica, *Ann. Glaciol.*, 41, 47–51, <https://doi.org/10.3189/172756405781813348>, 2005.

882 Johnson, J.S., Bentley, M.J., Smith, J.A., Finkel, R.C., Rood, D.H., Gohl, K., Balco, G.,
883 Larter, R.D. and Schaefer, J.M.: Rapid thinning of Pine Island Glacier in the early Holocene, *Science*,
884 343 (6174), 999–1001, <https://doi.org/10.1126/science.1247385>, 2014.

885 Johnson, J.S., Roberts, S.J., Rood, D.H., Pollard, D., Schaefer, J.M., Whitehouse, P.L.,
886 Ireland, L.C., Lamp, J.L., Goehring, B.M., Rand, C. and Smith, J.A.: Deglaciation of Pope Glacier
887 implies widespread early Holocene ice sheet thinning in the Amundsen Sea sector of Antarctica, *Earth
888 Planet Sc. Lett.*, 548, p.116501, <https://doi.org/10.1016/j.epsl.2020.116501>, 2020.

889 Johnson, J.S., Pollard, D., Whitehouse, P.L., Roberts, S.J., Rood, D.H. and Schaefer, J.M.:
890 Comparing glacial-geological evidence and model simulations of ice sheet change since the last

891 glacial period in the Amundsen Sea sector of Antarctica, *J. Geophys. Res.-Earth*, 126(6),
892 p.e2020JF005827, <https://doi.org/10.1029/2020JF005827>, 2021.

893 Johnson, J.S., Venturelli, R.A., Balco, G., Allen, C.S., Braddock, S., Campbell, S., Goehring,
894 B.M., Hall, B.L., Neff, P.D., Nichols, K.A. and Rood, D.H.: Existing and potential evidence for
895 Holocene grounding line retreat and readvance in Antarctica, *The Cryosphere*, 16 (5), 1543-1562,
896 <https://doi.org/10.5194/tc-16-1543-2022>, 2022.

897 Jones, R.S., Johnson, J.S., Lin, Y., Mackintosh, A.N., Sefton, J.P., Smith, J.A., Thomas, E.R.
898 and Whitehouse, P.L.: Stability of the Antarctic Ice Sheet during the pre-industrial Holocene, *Nat.
899 Rev. Earth Environ.*, 3, 500-515, <https://doi.org/10.1038/s43017-022-00309-5>, 2022.

900 Karlsson, N. B., Bingham, R. G., Rippin, D. M., Hindmarsh, R. C., Corr, H. F., and Vaughan,
901 D. G.: Constraining past accumulation in the central Pine Island Glacier basin, West Antarctica, using
902 radio-echo sounding, *J. Glaciol.*, 60, 553-562, <https://doi.org/10.3189/2014JoG13j180>, 2014.

903 Kausch, T., Lhermitte, S., Lenaerts, J., Wever, N., Inoue, M., Pattyn, F., Sun, S., Wauthy, S.,
904 Tison, J.L. and Van De Berg, W.J.: Impact of coastal East Antarctic ice rises on surface mass balance:
905 insights from observations and modeling, *The Cryosphere*, 14(10), pp.3367-3380,
906 <https://doi.org/10.5194/tc-14-3367-2020>, 2020.

907 Kingslake, J., Scherer, R.P., Albrecht, T., Coenen, J., Powell, R.D., Reese, R., Stansell, N.D.,
908 Tulaczyk, S., Wearing, M.G. and Whitehouse, P.L.: Extensive retreat and re-advance of the West
909 Antarctic Ice Sheet during the Holocene, *Nature*, 558 (7710), 430-434,
910 <https://doi.org/10.1038/s41586-018-0208-x>, 2018.

911 Koutnik, M.R., Fudge, T.J., Conway, H., Waddington, E.D., Neumann, T.A., Cuffey, K.M.,
912 Buijzer, C. and Taylor, K.C.: Holocene accumulation and ice flow near the West Antarctic Ice Sheet
913 Divide ice core site, *J. Geophys. Res.-Earth*, 121 (5), 907-924. <https://doi.org/10.1002/2015JF003668>,
914 2016.

915 Kurbatov, A.V., Zielinski, G.A., Dunbar, N.W., Mayewski, P.A., Meyerson, E.A., Sneed,
916 S.B. and Taylor, K.C.: A 12,000 year record of explosive volcanism in the Siple Dome Ice Core, West
917 Antarctica, *J. Geophys. Res.-Atmos*, 111 (D12). <https://doi.org/10.1029/2005JD006072>, 2006.

918 Le Brocq, A.M., Bentley, M.J., Hubbard, A., Fogwill, C.J., Sugden, D.E. and Whitehouse,
919 P.L.: Reconstructing the Last Glacial Maximum ice sheet in the Weddell Sea embayment, Antarctica,
920 using numerical modelling constrained by field evidence, *Quaternary Sci. Rev.*, 30(19-20), pp.2422-
921 2432, <https://doi.org/10.1016/j.quascirev.2011.05.009>, 2011.

922 Leysinger Vieli, G.J.M., Siegert, M.J. and Payne, A.J.: Reconstructing ice-sheet accumulation
923 rates at ridge B, East Antarctica, *Ann. Glaciol.*, 39, pp.326-330,
924 <https://doi.org/10.3189/172756404781814519>, 2004.

925 Leysinger Vieli, G.J.M., Hindmarsh, R.C., Siegert, M.J. and Bo, S.: Time-dependence of the
926 spatial pattern of accumulation rate in East Antarctica deduced from isochronic radar layers using a 3-
927 D numerical ice flow model, *J. Geophys. Res.-Earth*, 116 (F2), F02018,
928 <https://doi.org/10.1029/2010JF001785>, 2011.

929 Leysinger Vieli, G.M., Martin, C., Hindmarsh, R.C.A. and Lüthi, M.P., Basal freeze-on
930 generates complex ice-sheet stratigraphy, *Nat. Commun.*, 9(1), p.4669,
931 <https://doi.org/10.1038/s41467-018-07083-3>, 2018.

932 MacGregor, J.A., Matsuoka, K., Koutnik, M.R., Waddington, E.D., Studinger, M. and
933 Winebrenner, D.P.: Millennially averaged accumulation rates for the Vostok Subglacial Lake region

934 inferred from deep internal layers, Ann. Glaciol., 50 (51), 25-34.
935 <https://doi.org/10.3189/172756409789097441>, 2009.

936 MacGregor, J.A., Catania, G.A., Conway, H., Schroeder, D.M., Joughin, I., Young, D.A.,
937 Kempf, S.D. and Blankenship, D.D.: Weak bed control of the eastern shear margin of Thwaites
938 Glacier, West Antarctica, J. Glaciol., 59 (217), 900-912, <https://doi.org/10.3189/2013JoG13J050>,
939 2013.

940 MacGregor, J. A., Colgan, W. T., Fahnestock, M. A., Morlighem, M., Catania, G. A., Paden,
941 J. D., and Gogineni, S. P.: Holocene deceleration of the Greenland ice sheet, Science, 351 (6273),
942 590-593, <https://doi.org/10.1126/science.aab1702>, 2016.

943 MacGregor, J. A., Boisvert, L. N., Medley, B., Petty, A. A., Harbeck, J. P., Bell, R. E., Blair,
944 J. B., Blanchard-Wrigglesworth, E., Buckley, E.M., Christoffersen, M. S., and Cochran, J. R.: The
945 scientific legacy of NASA's Operation Icebridge, Rev. Geophys., 59, e2020RG000712,
946 <https://doi.org/10.1029/2020RG000712>, 2021.

947 Mayewski, P. A. and Dixon, D.A: US International TransAntarctic Scientific Expedition (US
948 ITASE) Glaciochemical Data, v. 2.0.0., NASA National Snow and Ice Data Center [data set],
949 <http://dx.doi.org/10.7265/N51V5BXR>, 2013.

950 ~~McConnell, J.R., Burke, A., Dunbar, N.W., Köhler, P., Thomas, J.L., Arienzo, M.M.,
951 Chellman, N.J., Maselli, O.J., Sigl, M., Adkins, J.F. and Baggensos, D.: Synchronous volcanic
952 eruptions and abrupt climate change ~ 17.7 ka plausibly linked by stratospheric ozone depletion, P.
953 Natl. A. Sci., 114 (38), 10035-10040, <https://doi.org/10.1073/pnas.1705595114>, 2017.~~

954 Medley, B., Joughin, I., Das, S.B., Steig, E.J., Conway, H., Gogineni, S., Criscitiello, A.S.,
955 McConnell, J.R., Smith, B.E., van den Broeke, M.R. and Lenaerts, J.T.: Airborne-radar and ice-core
956 observations of annual snow accumulation over Thwaites Glacier, West Antarctica confirm the
957 spatiotemporal variability of global and regional atmospheric models, Geophys. Res. Lett., 40(14),
958 pp.3649-3654, <https://doi.org/10.1002/grl.50706>, 2013.

959 Medley, B., Joughin, I., Smith, B.E., Das, S.B., Steig, E.J., Conway, H., Gogineni, S., Lewis,
960 C., Criscitiello, A.S., McConnell, J.R. and van den Broeke, M.R.: Constraining the recent mass
961 balance of Pine Island and Thwaites glaciers, West Antarctica, with airborne observations of snow
962 accumulation, The Cryosphere, 8 (4), 1375-1392, <https://doi.org/10.5194/tc-8-1375-2014>, 2014.

963 Morlighem, M.: MEaSUREs BedMachine Antarctica, v.2.0.0., NASA National Snow and Ice
964 Data Center Distributed Active Archive Center [data set], <https://doi.org/10.5067/E1QL9HFQ7A8M>,
965 2020.

966 Mouginot, J., Scheuchl, B., and Rignot, E.: MEaSUREs Antarctic Boundaries for IPY 2007-
967 2009 from Satellite Radar, v.2.0.0., NASA National Snow and Ice Data Center Distributed Active
968 Archive Center [data set], <http://dx.doi.org/10.5067/AXE4121732AD>, 2017.

969 Muldoon, G. R., Jackson, C. S., Young, D. A., and Blankenship, D. D.: Bayesian estimation
970 of englacial radar chronology in Central West Antarctica, Dynamics and Statistics of the Climate
971 System, 3(1), dzy004, <https://doi.org/10.1093/climatesystem/dzy004>, 2018.

972 Neuhaus, S.U., Tulaczyk, S.M., Stansell, N.D., Coenen, J.J., Scherer, R.P., Mikucki, J.A. and
973 Powell, R.D.: Did Holocene climate changes drive West Antarctic grounding line retreat and
974 readvance?, The Cryosphere, 15(10), 4655-4673, <https://doi.org/10.5194/tc-15-4655-2021>, 2021.

975 Neumann, T. A., Conway, H., Price, S. F., Waddington, E. D., Catania, G. A., and Morse, D.
976 L.: Holocene accumulation and ice sheet dynamics in central West Antarctica, J. Geophys. Res.-Earth,
977 113 (F2), F02018, <https://doi.org/10.1029/2007JF000764>, 2008.

1021 Steig, E.J., Fastook, J.L., Zweck, C., Goodwin, I.D., Licht, K.J., White, J.W. and Ackert Jr,
1022 R.P.: West Antarctic ice sheet elevation changes, *The West Antarctic Ice Sheet: Behavior and*
1023 *Environment*, 77, 75-90. <https://doi.org/10.1029/AR077p0075>, 2001.

1024 Stone, J.O., Balco, G.A., Sugden, D.E., Caffee, M.W., Sass III, L.C., Cowdery, S.G. and
1025 Siddoway, C.: Holocene deglaciation of Marie Byrd land, west Antarctica, *Science*, 299 (5603), 99-
1026 102, <https://doi.org/10.1126/science.1077998>, 2003.

1027 Suganuma, Y., Miura, H., Zondervan, A. and Okuno, J.I.: *East Antarctic deglaciation and the*
1028 *link to global cooling during the Quaternary: Evidence from glacial geomorphology and 10Be surface*
1029 *exposure dating of the Sør Rondane Mountains, Dronning Maud Land, Quaternary Sci. Rev.*, 97,
1030 *pp.102-120, https://doi.org/10.1016/j.quascirev.2014.05.007*, 2014.

1031 Sutter, J., Fischer, H. and Eisen, O.: Investigating the internal structure of the Antarctic ice
1032 sheet: the utility of isochrones for spatiotemporal ice-sheet model calibration, *The Cryosphere*, 15 (8),
1033 3839-3860. <https://doi.org/10.5194/tc-15-3839-2021>, 2021.

1034 RAISED Consortium: *A community-based geological reconstruction of Antarctic Ice Sheet*
1035 *deglaciation since the Last Glacial Maximum*, *Quaternary Sci. Rev.*, 100, pp.1-9.
1036 <https://doi.org/10.1016/j.quascirev.2014.06.025>, 2014.

1037 yVan Den Broeke, M.R. and yVan Lipzig, N.P.: Changes in Antarctic temperature, wind and
1038 precipitation in response to the Antarctic Oscillation, *Ann. Glaciol*, 39, 119-126,
1039 <https://doi.org/10.3189/172756404781814654>, 2004.

1040 Van Wessem, J.M., Van De Berg, W.J., Noël, B.P., Van Meijgaard, E., Amory, C., Birnbaum,
1041 G., Jakobs, C.L., Krüger, K., Lenaerts, J., Lhermitte, S. and Ligtenberg, S.R.: Modelling the climate
1042 and surface mass balance of polar ice sheets using RACMO2-Part 2: Antarctica (1979–2016), *The*
1043 *Cryosphere*, 12 (4), 479-1498, <https://doi.org/10.5194/tc-12-1479-2018>, 2018.

1044 Vaughan, D.G., Corr, H.F., Ferraccioli, F., Frearson, N., O'Hare, A., Mach, D., Holt, J.W.,
1045 Blankenship, D.D., Morse, D.L. and Young, D.A.: New boundary conditions for the West Antarctic
1046 ice sheet: Subglacial topography beneath Pine Island Glacier, *Geophys. Res. Lett.*, 33 (9), L09501,
1047 <https://doi.org/10.1029/2005GL025588>, 2006.

1048 Venturelli, R.A., Siegfried, M.R., Roush, K.A., Li, W., Burnett, J., Zook, R., Fricker, H.A.,
1049 Priscu, J.C., Leventer, A. and Rosenheim, B.E.: Mid-Holocene grounding line retreat and readvance
1050 at Whillans Ice Stream, West Antarctica, *Geophys. Res. Lett.*, 47 (15), p.e2020GL088476,
1051 <https://doi.org/10.1029/2020GL088476>, 2020.

1052 Waddington, E. D., Neumann, T. A., Koutnik, M. R., Marshall, H.-P., and Morse, D. L.:
1053 Inference of accumulation-rate patterns from deep layers in glaciers and ice sheets, *J. Glaciol.*, 53
1054 (183), 694–712, <https://doi.org/10.3189/002214307784409351>, 2007.

1055 WAIS Divide Project Members: Onset of deglacial warming in West Antarctica driven by
1056 local orbital forcing, *Nature*, 500 (7463), 440-444, <https://doi.org/10.1038/nature12376>, 2013.

1057 Wearing, M.G. and Kingslake, J.: Holocene Formation of Henry Ice Rise, West Antarctica,
1058 Inferred from Ice-Penetrating Radar, *J. Geophys. Res.-Earth*, 124 (8), 2224-2240,
1059 <https://doi.org/10.1029/2018JF004988>, 2019.

1060 Whillans, I. M.: Radio-echo layers and the recent stability of the West Antarctic ice sheet,
1061 *Nature*, 264, 5582, 152, <https://doi.org/10.1038/264152a0>, 1976.

1062 Winter, A., Steinhage, D., Creyts, T.T., Kleiner, T. and Eisen, O.: Age stratigraphy in the East
1063 Antarctic Ice Sheet inferred from radio-echo sounding horizons, *Earth Syst. Sci. Data*, 11 (3), 1069-
1064 1081, <https://doi.org/10.5194/essd-11-1069-2019>, 2019.

High mid-Holocene accumulation rates over West Antarctica inferred from a pervasive ice-penetrating radar reflector

Julien A. Bodart¹, Robert G. Bingham¹, Duncan A. Young², Joseph A. MacGregor³, David W. Ashmore^{4,7}, Enrica Quartini^{2,5}, Andrew S. Hein¹, David G. Vaughan^{6†}, and Donald D. Blankenship²

Supplementary Information

Assessing the suitability of the local-layer approximation

To quantify to what extent the assumptions used in the 1-D model are valid for estimating Holocene accumulation rates between the 4.72 ka IRH and the present, we calculated horizontal gradients in modern ice thickness and accumulation rates over the WAIS, and combined these to calculate the non-dimensional parameter D spanning the catchments where the 4.72 ka IRH was traced (Waddington et al., 2007) (Fig. S1).

The input datasets used for this calculation were modern ice thickness from BedMachine v2 (Morlighem, 2020), modern surface mass balance (1979 – 2019) from RACMO 2.3p2 (Van Wessem et al., 2018), and modern surface velocities (1996 – 2016) from the InSAR MEaSUREs v2 dataset (Rignot et al., 2017). These were all re-gridded to a single 1-km grid using bilinear interpolation and smoothed using an exponentially decaying filter equivalent to ten ice thicknesses in length, before subsampling the data to a common 5-km grid for data analysis. Following MacGregor et al. (2016), we re-calculated surface speed directions for slower ice-flow regions ($<100 \text{ m a}^{-1}$) in the interior of the ice sheet using surface-elevation gradients from the BedMachine product. To calculate L_{path} (Fig. S1a), we then produced a reverse flowline for each grid cell based on modern ice-surface velocity, \bar{u} , and calculated where along the reverse flowline we obtained age, a , as follows:

$$L_{path} = \bar{u} a. \quad (\text{S1})$$

We then interpolated the ice-thickness and accumulation-rate grids onto each flowline and conducted a first-order polynomial fit to obtain the ice-thickness and accumulation gradients along the flowline. The ensuing gradients were then combined with the mean values along the flowline (\bar{H} and \bar{b}) to calculate the characteristic lengths L_H and L_b (Fig. S1b-c), as follows:

$$\frac{1}{L_H} = \left| \frac{1}{\bar{H}} \frac{dH}{dx} \right| \text{.} \quad (\text{S2})$$

$$\frac{1}{L_b} = \left| \frac{1}{\bar{b}} \frac{db}{dx} \right| \text{.} \quad (\text{S3})$$

Taken together, the ice-thickness and accumulation-rate gradients were combined to obtain a characteristic length scale, which was used to compare with L_{path} to generate the non-dimensional parameter D (Fig. S1d):

$$D = L_{path} \left(\frac{1}{L_H} + \frac{1}{L_b} \right). \quad (S4)$$

Values where $D \ll 1$ indicate that local horizontal gradients in ice thickness and accumulation rates have a smaller effect on IRH depth of age a , and hence we assume that the LLA is valid for estimating accumulation rates for an IRH of age a (Waddington et al., 2007; MacGregor et al., 2009) (Sect. 2.2.1).

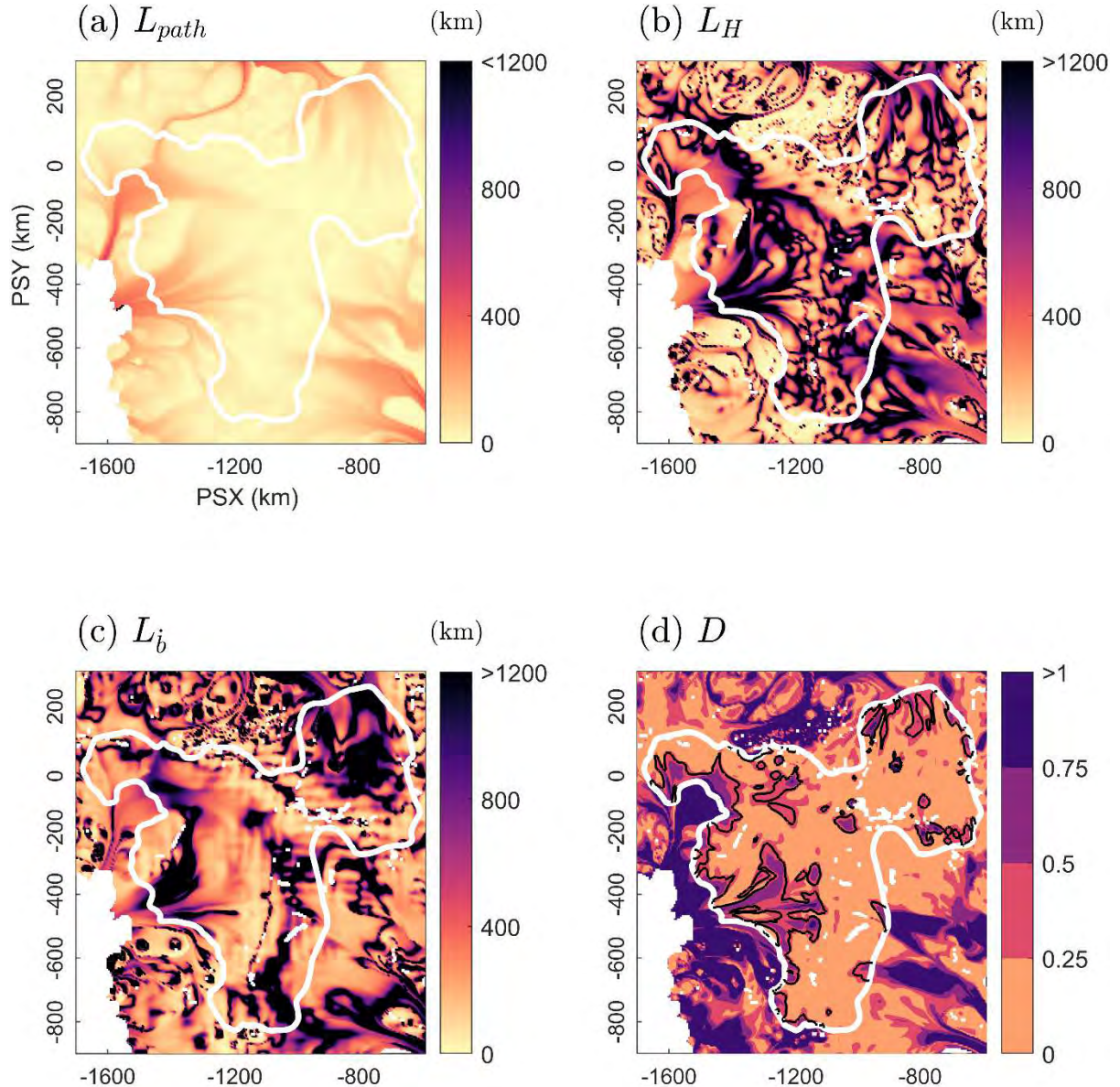


Figure S1. Suitability of the Local-Layer Approximation over the Pine Island, Thwaites, Institute and Möller ice-stream catchments for the 4.72 ka IRH. (a) Horizontal path length of a 4.72 ka particle of ice to reach its present location, calculated using modern surface velocities (Rignot et al., 2017). (b) Characteristic length of ice-thickness variability along the 4.72 ka particle path, estimated using modern ice thickness measurements from BedMachine v2 (Morlighem, 2020). (c) Characteristic length of accumulation variability along the 4.72 ka particle path, estimated using modern modelled surface mass balance data from RACMO2 (Van Wessem et al., 2018). (d) The D parameter for the 4.72 ka IRH used to quantify the suitability of the LLA for the survey area. The white outline represents the model domain boundary used to model Holocene accumulation rates where D

≤ 1 , whereas the black outline represents the upper limit of the interquartile range for the D parameter (i.e. $D \leq 0.34$) which we use to assess the level of confidence in the inferred Holocene accumulation rates.

Estimating uncertainty in inferred accumulation rates

Because the Nye model does not directly take into account the effect of strain rates on IRH depth and position within the ice column, it is not possible to assess its impact on the inferred accumulation rates, particularly in areas where strain rates are higher and the IRHs are deeper in the ice (e.g. the downstream section of our grid where ice flow is faster; Figs. 1-2 of the main paper). In turn, this limits our ability to quantify the model's structural uncertainty. Because the [structural model](#) uncertainty is likely larger than that related to the IRH age (Section 2.2 of the main paper), it is important to quantify it to assess the significance of accumulation-rate change from modern values that we detect.

To overcome this issue, we used the shallow-strain rate model developed by MacGregor et al. (2016) which includes a strain-rate parameter directly that is independent from ice thickness, rather than one that is tied to ice thickness as in the Nye model. The accumulation rates produced by this model are then used here to estimate lower and upper bounds in the accumulation rates that partly consider the effect of non-Nye vertical strain on the ice column and thus on the accumulation rate needed to reproduce the depth of the 4.72 ka IRH in the Nye model. The [shallow-strain rate model](#) is:

$$a(z) = \frac{1}{\dot{\varepsilon}_{zz}^a} \ln \left(\frac{\dot{b}_a + \dot{\varepsilon}_{zz}^a z_a}{\dot{b}_a} \right). \quad (\text{Eq. S5})$$

The strain-rate parameter in Eq. (S5) would typically be $\dot{\varepsilon}_{zz}^a$ from Figure S2a, but because this is calculated based on the results from Eq. (1) it is not independent from the inferred accumulation rates presented here and is thus not a suitable input for evaluating accumulation-rate uncertainty inferred from the Nye model. In the absence of well-constrained vertical strain rates across our grid, by continuity, we used the longitudinal strain rates ($\dot{\varepsilon}_{xx}$; Fig. S2b) as an alternative to $\dot{\varepsilon}_{zz}^a$ in the shallow-strain rate model (ignoring lateral strain).

These were calculated from gradients in the x and y-direction for modern surface speeds (\bar{u}) projected onto the appropriate surface velocity unit vectors ($\hat{u}_{||}$) (MacGregor et al., 2013):

$$\dot{\varepsilon}_{xx} = \frac{\partial u}{\partial x} = \bar{\nabla} |\bar{u}| \cdot \hat{u}_{||}. \quad (\text{Eq. S6})$$

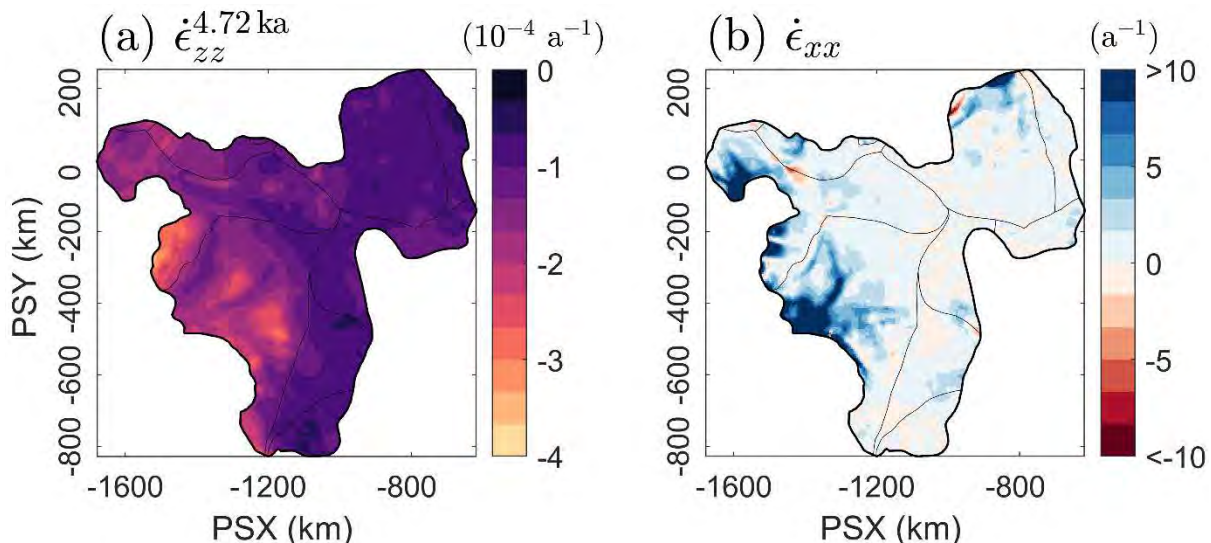


Figure S2. Strain rate patterns across the survey area. (a) Mean Nye-inferred vertical strain rates, $\dot{\varepsilon}_{zz}^a$, for the 0-4.72 ka portion of the ice column calculated from Eq. (2) (b) Longitudinal strain rates, $\dot{\varepsilon}_{xx}$, obtained from Eq. (S6).

To assess whether $\dot{\varepsilon}_{xx}$ can be used as a proxy for $\dot{\varepsilon}_{zz}^a$, we solved Eq. S5 for \dot{b}_a , replaced $\dot{\varepsilon}_{zz}^a$ for $\dot{\varepsilon}_{xx}$, and then compared the accumulation rate results inferred from the shallow-strain model to the Nye-inferred accumulation rates over our grid from Figure 3a. Note that $\dot{\varepsilon}_{xx}$ can only be used as a proxy for $\dot{\varepsilon}_{zz}^a$ where $\dot{\varepsilon}_{xx} > 0$, as positive $\dot{\varepsilon}_{zz}^a$ values are typically only found in areas where the ice column is expanding, such as the ablation zone, and are thus non-physical for our model domain. As a result, all negative $\dot{\varepsilon}_{xx}$ values were replaced by extremely low but positive strain-rate values (10^{-7} a^{-1}). The results shown in Figure S3 demonstrate that both the Nye and shallow-strain models produce similar results, but with decreasing similarity where $D > 0.34$, which is likely related to ice-dynamical processes affecting the assumptions of the Nye model further downstream (Fig. S4).

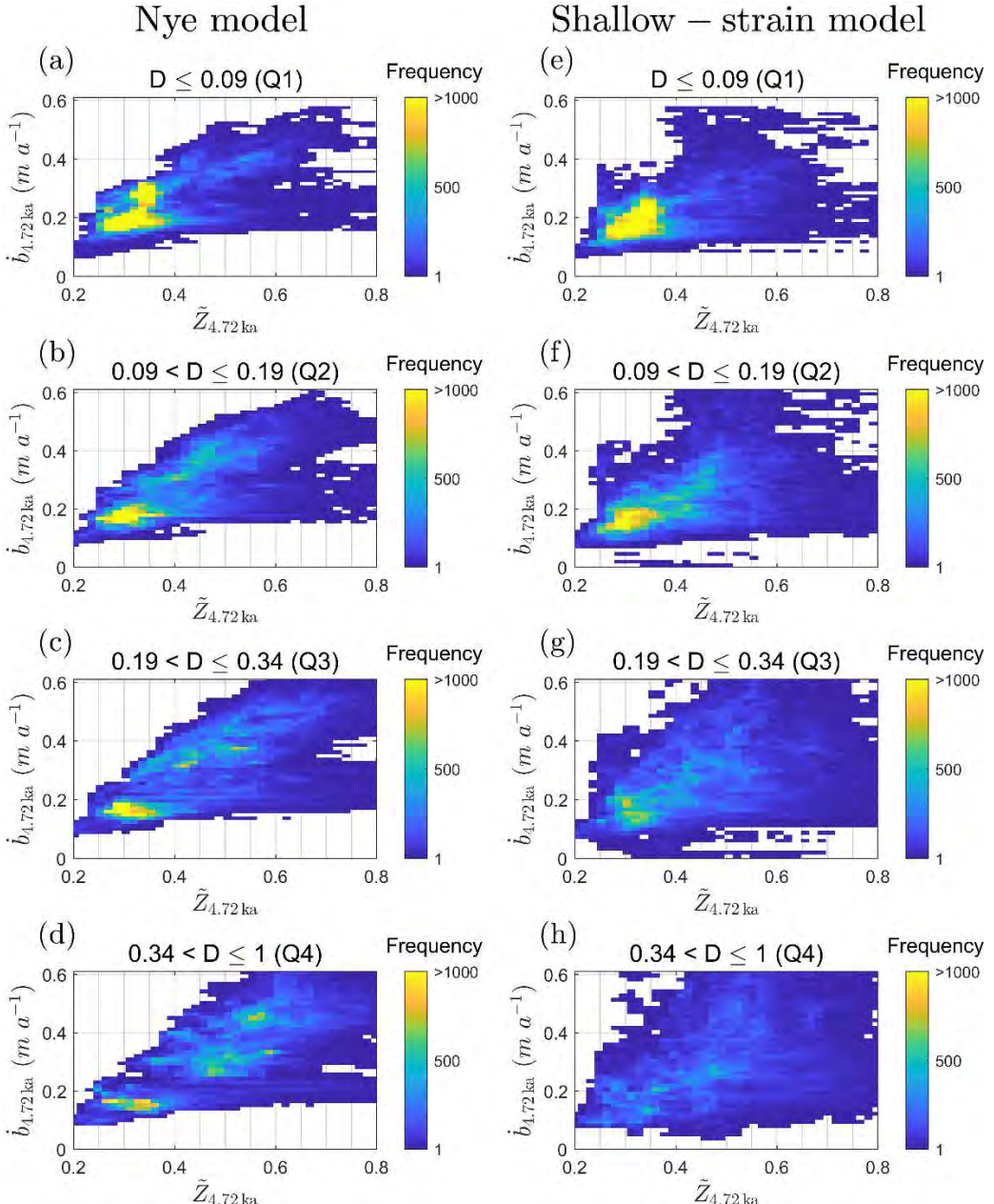


Figure S3. Histograms of inferred accumulation rates from the Nye (a-d) and shallow-strain rates (e-h) models plotted against normalised IRH depths and binned into the four D quartiles (e.g. panels a and e are for all

grid cells that fall within the lower quartile (Q1), b and f for all those that fall within the second quartile (Q2), etc; Sect. 2.2.1 of the main paper).

This analysis increases confidence that $\dot{\varepsilon}_{xx}$ can be used in the shallow-strain rate model from MacGregor et al. (2016) as a proxy for the vertical strain parameter, $\dot{\varepsilon}_{zz}^a$, to infer accumulation rates over the time period and location considered here, and thus ultimately has value for constraining uncertainty in the Nye-inferred accumulation rates (Fig. 3a). While this method likely produces more conservative uncertainty estimates than with the more challenging use of inverse flowband models that solves for the effect of changing flow, temperature and strain conditions along targeted flowbands, it enables a straightforward uncertainty quantification across a large area.

We then produced two sets of upper and lower accumulation-rate uncertainties ($\dot{b}_{4.72 \text{ ka}}^{\text{Low}}$ and $\dot{b}_{4.72 \text{ ka}}^{\text{High}}$) for each of the following products over our grid: (1) using the Nye model from Eq. 1 with the IRH age uncertainty ($\pm 0.28 \text{ ka}$); and (2) same as (1) but using the shallow strain-rate model from Eq. S5 using $\dot{\varepsilon}_{xx}$ as a proxy for $\dot{\varepsilon}_{zz}^a$. We then calculated the maximum $\dot{b}_{4.72 \text{ ka}}^{\text{Low}}$ and $\dot{b}_{4.72 \text{ ka}}^{\text{High}}$ values for each grid cell (Fig. S4a-b) and combined these to provide a relative uncertainty to the Nye-inferred accumulation rates (Fig. S4c). The largest relative uncertainties to the Nye-inferred accumulation rates ($> 70\%$) are found primarily across the downstream end of Thwaites Glacier, and to a smaller extent over the edges of the grid of Pine Island Glacier and Institute and Möller Ice Streams where longitudinal strain rates are higher due to faster flowing ice. Relatively low uncertainties are found across the Amundsen-Weddell-Ross divide and most of the region where $D \leq 0.34$.

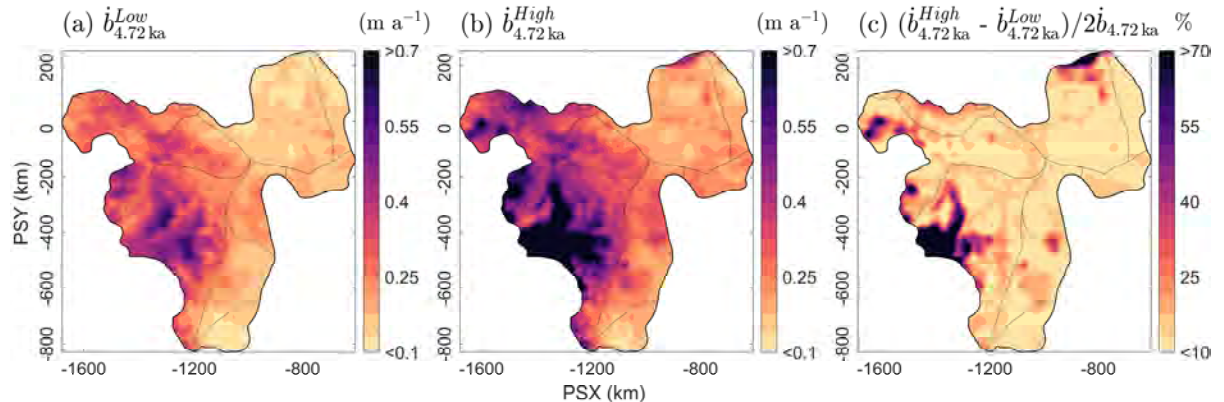


Figure S4. Uncertainties in inferred accumulation rates based on the radar and ice-core age uncertainties and from the accumulation rates returned from the shallow-strain rate model (Eq. S5). (a) Lower bound accumulation estimates, which are the product combination of the combined uncertainty from the radar and ice-core uncertainties in the age of the $4.72 \pm 0.28 \text{ ka}$ IRH (Muldoon et al., 2018; Bodart et al., 2021) and the accumulation rate returned from the shallow-strain rate model. (b) same as (a) but for the upper bounds in accumulation rates. (c) Relative uncertainty in Nye-inferred accumulation rates for the 4.72 ka IRH (Fig. 3a) based on the lower and upper bound estimates from Figures S4a-b.

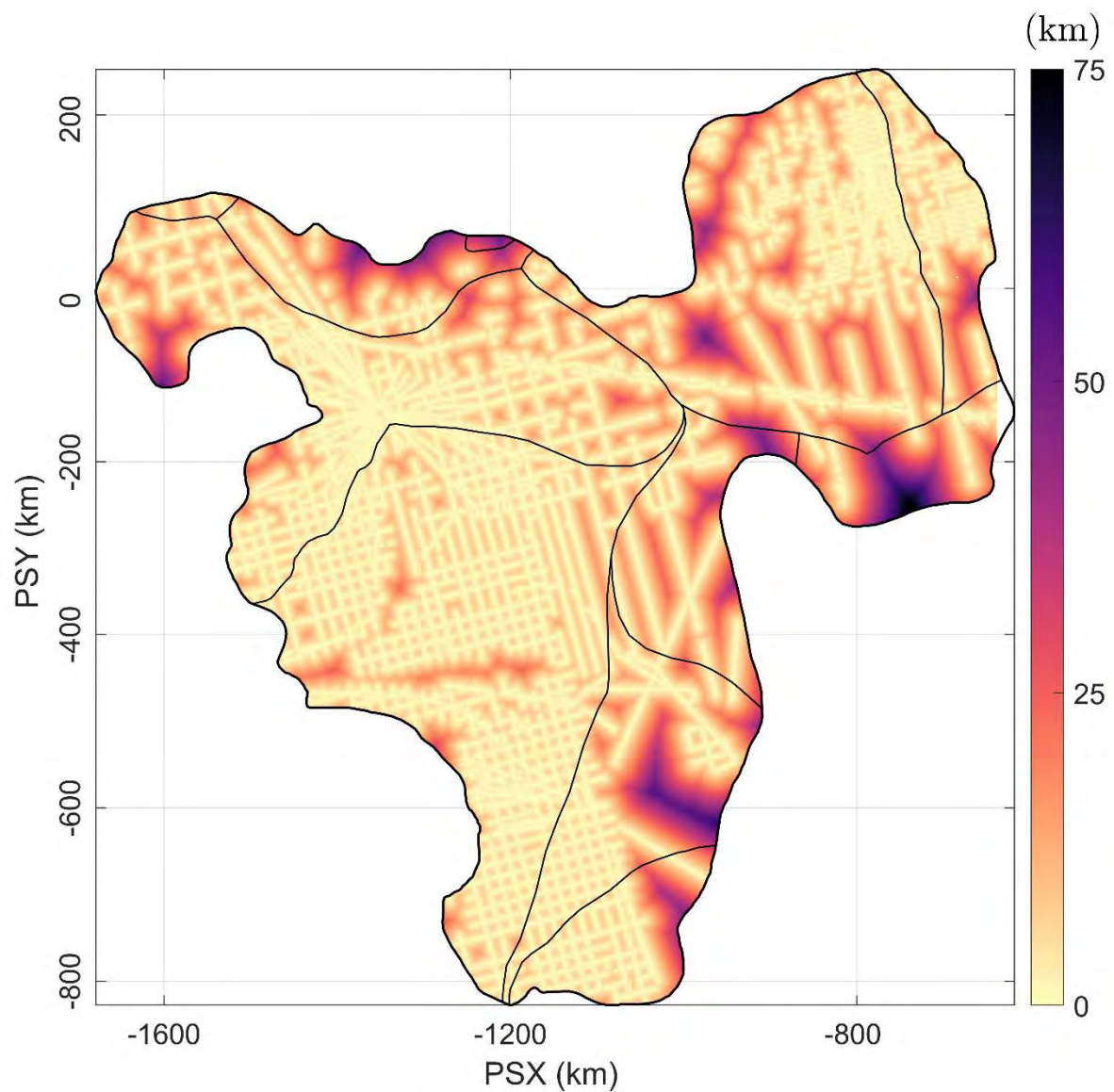


Figure S5. Maximum distance to the nearest 500-m along-track point used for the interpolation of the 4.72 ka IRH depth and accumulation grids.

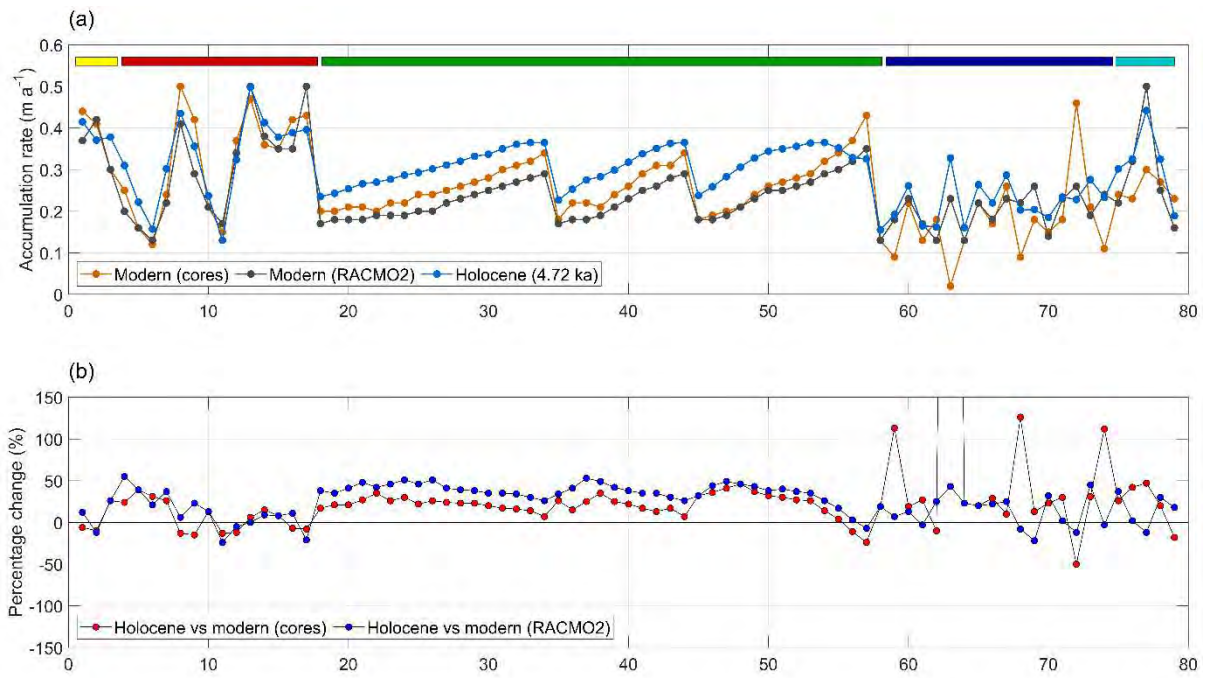


Figure S6. Scatter plot showing the difference in accumulation rates between the modern (cores and RACMO2) and the Holocene (4.72 ka) based on data showed in Figures 3c and 4 of the main paper. (a) Accumulation rates for each of Modern (cores), Modern (RACMO2), and Holocene (4.72 ka) at each of the 79 core locations shown in Figure 1. The five colour boxes at the top of (a) indicate the datasets to which each point belongs and are colour-coded as per the legend in Figure 1 (from left to right: MED14, ITASE, NEU08, SAMBA, SEAT-10). (b) Percentage change between Holocene and modern (cores; red) and Holocene and modern (RACMO2; blue) at the 79 core locations shown in Figure 1.